Evidence of First Stars-enriched Gas in High-redshift Absorbers*

Andrea Saccardi, Stefania Salvadori, Valentina D'odorico, Guido Cupani, Michele Fumagalli, Trystyn a M Berg, George D Becker, Sara Ellison, Sebastian Lopez

To cite this version:

Andrea Saccardi, Stefania Salvadori, Valentina D'odorico, Guido Cupani, Michele Fumagalli, et al.. Evidence of First Stars-enriched Gas in High-redshift Absorbers*. The Astrophysical Journal, 2023, 948 (1), pp.35. ⟨10.3847/1538-4357/acc39f⟩. ⟨insu-04091981⟩

HAL Id: insu-04091981
https://insu.hal.science/insu-04091981v1

Submitted on 9 May 2023

THE ASTROPHYSICAL JOURNAL, 948:35 (16pp), 2023 May 1 https://doi.org/10.3847/1538-4357/acc39f

Evidence of First Stars-enriched Gas in High-redshift Absorbers*

Andrea Saccardi[1,2], Stefania Salvadori[2,3], Valentina D'Odorico[4,5,6], Guido Cupani[5,6], Michele Fumagalli[7,5], Trystyn A. M. Berg[7], George D. Becker[8], Sara Ellison[9], and Sebastian Lopez[10]

[1] GEPI, Observatoire de Paris, Université PSL, CNRS, 5 Place Jules Janssen, F-92190 Meudon, France; andrea.saccardi@obspm.fr
[2] Dipartimento di Fisica e Astronomia, Università degli Studi di Firenze, Via G. Sansone 1, I-50019 Sesto Fiorentino, Italy
[3] INAF—Osservatorio Astrofisico di Arcetri, Largo E. Fermi 5, I-50125 Firenze, Italy
[4] Scuola Normale Superiore, Piazza dei Cavalieri 7, I-56126 Pisa, Italy
[5] INAF—Osservatorio Astronomico di Trieste, via G.B. Tiepolo, 11 I-34143 Trieste, Italy
[6] IFPU—Institute for Fundamental Physics of the Universe, Via Beirut 2, I-34014 Trieste, Italy
[7] Dipartimento di Fisica G. Occhialini, Università degli Studi di Milano Bicocca, Piazza della Scienza 3, I-20126 Milano, Italy
[8] Department of Physics & Astronomy, University of California, Riverside, CA 92521, USA
[9] Department of Physics & Astronomy, University of Victoria, Finnerty Road, Victoria, BC V8P 1A1, Canada
[10] Departamento de Astronomía, Universidad de Chile, Casilla 36-D, Santiago, Chile

Received 2022 November 28; revised 2023 February 22; accepted 2023 February 26; published 2023 May 3

Abstract

The first stars were born from chemically pristine gas. They were likely massive, and thus they rapidly exploded as supernovae, enriching the surrounding gas with the first heavy elements. In the Local Group, the chemical signatures of the first stellar population were identified among low-mass, long-lived, very metal-poor ([Fe/H] < -2) stars, characterized by high abundances of carbon over iron ([C/Fe] $> +0.7$): the so-called carbon-enhanced metal-poor stars. Conversely, a similar carbon excess caused by first-star pollution was not found in dense neutral gas traced by absorption systems at different cosmic time. Here we present the detection of 14 very metal-poor, optically thick absorbers at redshift $z \sim 3$–4. Among these, 3 are carbon-enhanced and reveal an overabundance with respect to Fe of all the analyzed chemical elements (O, Mg, Al, and Si). Their relative abundances show a distribution with respect to [Fe/H] that is in very good agreement with those observed in nearby very metal-poor stars. All the tests we performed support the idea that these C-rich absorbers preserve the chemical yields of the first stars. Our new findings suggest that the first-star signatures can survive in optically thick but relatively diffuse absorbers, which are not sufficiently dense to sustain star formation and hence are not dominated by the chemical products of normal stars.

Unified Astronomy Thesaurus concepts: Chemical abundances (224); Quasar absorption line spectroscopy (1317); Metallicity (1031)

Supporting material: figure set, machine-readable table

1. Introduction

Cosmological simulations show that the first (Population III) stars are likely more massive than present-day "normal" stars, with a characteristic mass of $\sim 10\,M_\odot$ and a maximum mass possibly extending up to $\sim 1000\,M_\odot$ (e.g., Hosokawa et al. 2011; Hirano et al. 2014). Among such a variety of stellar masses there are many channels to produce supernovae (SNe) and thus to contaminate the surrounding environment with the heavy elements newly produced by Population III stars. Very massive first stars, $140\ M_\odot \leqslant M_{\rm PopIII} \leqslant 260\ M_\odot$, explode as pair-instability SNe yielding chemical abundance ratios that exhibit a strong odd–even effect (Heger & Woosley 2002; Takahashi et al. 2018) and a unique lack of cobalt and zinc over iron (Salvadori et al. 2019). First stars with intermediate masses, $10\ M_\odot \leqslant M_{\rm PopIII} \leqslant 100\ M_\odot$, also evolve as SNe, but they can have a variety of explosion energies, thus yielding very different chemical element ratios depending on the mass of the progenitor star and the SN explosion energy (see e.g., Heger & Woosley 2010; Limongi & Chieffi 2018, for theory; and Placco et al. 2021; Skúladóttir et al. 2021, for observations). Low-mass stars, born from the gas polluted by first stars (Bromm & Loeb 2003; Schneider et al. 2003), can survive until the present day and retain in their atmospheres a record of the chemical elements produced by these first stars.

The search for the chemical signatures of Population III stars has focused on ancient metal-poor stars in our cosmic neighborhood. In particular, stars in the Milky Way (MW) halo and Local Group dwarf galaxies are prime targets, as we can uniquely study individual stars (e.g., Beers & Christlieb 2005; Frebel & Norris 2015; Simon 2019). Historically a new class of carbon-enhanced metal-poor (CEMP) stars was first recognized from the observations of Beers et al. (1992). A few years later two simultaneous studies, by Norris et al. (1997) and Bonifacio et al. (1998), identify for the first time an object pertaining to the class of CEMP-no stars, i.e., stars that are very metal-poor ([Fe/H] < -2), strongly enhanced in carbon with respect to iron ([C/Fe] $> +0.7$), and not enriched in neutron-capture elements ([Ba/Fe] < 0.0). At the moment many CEMP-no stars have been discovered (e.g., Christlieb et al. 2002; Rossi et al. 2005; Norris et al. 2013; Bonifacio et al. 2015; Aguado et al. 2022; Zepeda et al. 2022), and very recently it has been confirmed by Aguado et al. (2023) that these objects are most likely the descendants of massive first stars that exploded as low-energy SNe (e.g., Iwamoto et al. 2005; Marassi et al. 2014).

---

* Based on data products from the XQ-100 survey made with ESO Telescopes at the La Silla Paranal Observatory under programme ID 189.A-0424.

Indeed, when the explosion energy of an SN is not high enough to expel Fe-peak elements from the innermost layers, a large fraction of them fall back onto the remnant (e.g., Heger & Woosley 2010). During these faint SN explosions, therefore, only the outermost layers rich in carbon and other light elements are ejected, yielding large values of [C/Fe]. The idea that CEMP-no stars formed in an environment polluted by low-energy primordial SNe is further supported by the increasing frequency of CEMP-no stars toward lower [Fe/H] (e.g., Beers & Christlieb 2005; Marsteller et al. 2005; Lucatello et al. 2006; Lee et al. 2013; Placco et al. 2014; de Bennassuti et al. 2017; Yoon et al. 2018; Liu et al. 2021).

Among the very metal-poor stars enriched with carbon, another population exists: stars that exhibit an excess in heavy elements formed by slow (or rapid) neutron-capture processes, dubbed CEMP-*s* (or CEMP-*r*) stars. The available data suggest that most CEMP-*s* stars dwell in binary systems (Lucatello et al. 2005; Starkenburg et al. 2014; Hansen et al. 2016b; Arentsen et al. 2019) and thus that their carbon excess is not inherited from the natal cloud but acquired via mass transfer. The surplus of carbon likely comes from an evolved star that has passed through the asymptotic giant branch (AGB) phase (Abate et al. 2015), during which *s*-elements are also produced (Karakas & Lattanzio 2014). On the other hand, the carbon excess in CEMP-no stars is expected to be representative of the environment of formation (e.g., Hansen et al. 2016a; Zepeda et al. 2022), even in the rare case in which CEMP-no stars are found to dwell in binary systems (Aguado et al. 2022, 2023).

Based on these results from ancient nearby stars, we expect that at high redshifts it could be possible to find very metal-poor gaseous environments primarily enriched by the first stars (Pallottini et al. 2014), thus showing a carbon excess.

Quasar absorption lines provide an important gateway to infer observational constraints on galaxy formation and evolution and to look for the signatures of the first stars in gas at high-redshifts. Detecting gas exhibiting similar abundance patterns as CEMP-no stars would open a new window to investigate the properties of the first stars and galaxies in the early universe. Yet, despite long searches at $z > 2$–3, this distinctive chemical signature has not been discovered in dense absorbers (Cooke et al. 2011b; Dutta et al. 2014), such as damped Lyα systems (DLAs). These DLAs, which have neutral hydrogen column density $\log(N_{\rm H\,I}/{\rm cm}^{-2}) > 20.3$, trace most of the neutral gas in the universe, together with the galaxies' interstellar medium (ISM).

A claim of detection of a CEMP-DLA (QSO J0035−0918) at $z_{\rm abs} = 2.340$ with $[{\rm Fe/H}] = -3.04$ and $[{\rm C/Fe}] = +1.53$ was published by Cooke et al. (2011a). However, two subsequent works have disproved the result, reporting a much lower carbon-to-iron ratio for the same DLA absorption system, i.e., respectively equal to $[{\rm C/Fe}] = +0.51 \pm 0.10$ and $[{\rm C/Fe}] = +0.45 \pm 0.19$ (Carswell et al. 2012; Dutta et al. 2014). Another DLA with $[{\rm C/Fe}] = +0.59$, $[{\rm Fe/H}] = -2.84$ at $z = 3.07$ has been reported by Cooke et al. (2012), which is, however, below the limit value of $[{\rm C/Fe}] = +0.7$. Two recent works (Welsh et al. 2019, 2022) presenting a collection of all the very metal-poor DLAs in the literature confirm the absence of carbon-enhancement claims.

Aiming at detecting the chemical evidence of gas enriched by the first stars, Lyman limit systems (LLSs) and sub-damped Lyα systems (sub-DLAs), with $17.2 \leqslant \log(N_{\rm H\,I}/{\rm cm}^{-2}) \leqslant 20.3$, represent promising gaseous environments to look for the fingerprints of Population III stars. Indeed, they are less dense than DLAs and therefore metal-poorer (Fumagalli et al. 2016) and likely not strongly contaminated by subsequent generations of normal (Population II) stars (Salvadori & Ferrara 2012), which are expected to form early on in the ISM of Population III enriched galaxies. On the other hand, these systems trace optically thick, relatively diffuse gas that is not sufficiently dense to self-shield the UV radiation; consequently, they are likely characterized by more complex ionization patterns.

In this work, we exploited the XQ-100 quasar legacy survey (López et al. 2016) to collect a sample of 54 absorption systems at redshift $z \sim 3$–4 selected by the presence of the Mg II absorption doublet. Among these systems, we identified a subsample of 37 diffuse optically thick LLSs and sub-DLAs absorbers that we have studied in detail. We performed Voigt profile fitting of metal absorption features and hydrogen Lyman lines in the quasar spectra to measure column densities. To derive relative abundances of different elements, we applied photoionization model corrections to the measured ionic abundances.

In Section 2 we present our data set, including the line profile fitting of the absorption systems and the determination of the chemical abundances. In Sections 3 and 4 we present and discuss the results. The conclusions are drawn in Section 5.

2. Data Analysis

The Large Programme "Quasars and Their Absorption Lines: A Legacy Survey of the High-redshift Universe with (VLT)/X-shooter" (López et al. 2016) has produced a homogeneous and high-quality sample of echelle spectra of 100 quasars (QSOs) with emission redshift $z \sim 3.5$–4.5. The targets were observed with the X-shooter spectrograph (Vernet et al. 2011) mounted at the ESO Very Large Telescope (VLT, Cerro Paranal, Chile). X-shooter is characterized by three arms that allow us to cover in one observation the full spectral range between the atmospheric cutoff at 300 nm and the near-infrared *K*-band at 2500 nm, at an intermediate resolving power. The full spectral coverage, along with a well-defined target selection and the high signal-to-noise ratio (S/N) achieved (median S/N = 30), clearly makes XQ-100 a unique data set to study the rest-frame UV/optical spectra of high-z QSOs in a single, homogeneous, and statistically significant sample. The adopted slit widths were 1.″0 in the UVB arm and 0.″9 in the VIS and NIR arms, to match the requested seeing and to account for its wavelength dependence. These slit widths provide nominal resolving powers of 5400, 8900, and 5600 for the UVB, VIS, and NIR arms, respectively.[11] The XQ-100 survey was designed to cover many science cases: from the detailed study of the intergalactic medium to the detection of galaxies in absorption (Berg et al. 2016; Sánchez-Ramírez et al. 2016; Christensen et al. 2017), from the properties of QSO themselves (Perrotta et al. 2016, 2018) to cosmology (Iršič et al. 2017a, 2017b). The spectra, reduced from the collaboration, were delivered to the public.[12] Two types of reduced data are provided for each target: (i) a joint spectrum of the three arms together; and (ii) individual UVB, VIS, and NIR arm spectra, which includes telluric correction and fitted QSO continuum. When a target is observed more than once at different epochs, there is one spectrum for each

---

[11] The nominal resolutions are different from those of López et al. (2016) since at that time, due to a problem in X-shooter's data reduction, the resolutions were calculated incorrectly. https://www.eso.org/sci/facilities/paranal/instruments/xshooter.html.

[12] https://www.eso.org/qi/catalog/show/73

epoch and a combined spectrum, putting together all epochs. The telluric corrections are calculated on the spectra corresponding to the single epochs, while the continuum is calculated only on the combined spectrum.

Since for our purposes we needed telluric-corrected spectra, we created a coadded spectrum when multiple observations were present, and then we redetermined the intrinsic QSO continuum in the framework of the *Astrocook*[13] Python software package (Cupani et al. 2020). In *Astrocook*, the emission continuum is estimated by first masking the most prominent absorption features and then interpolating the nonmasked regions with a univariate spline of chosen degree.

The final spectrum for each QSO was created by cutting the noisy edges of each arm and "stitching" the three arms together. Also these operations were carried out using *Astrocook*.

Before creating the final spectra, we estimated the "effective" resolving power determined by the atmospheric conditions during observations. Indeed, if the seeing during observations is smaller than the width of the slit, the "effective" resolving power of the obtained spectrum will be larger than the nominal one. We recomputed the value of the resolving power (R) for each spectrum (Table 1) based on the average value of the seeing during the observations (reported in the ESO archive as DIMM) and assuming a linear relation between resolving power and slit width. For example, in the VIS arm, if $\langle\mathrm{DIMM}\rangle < 0\farcs9$, the new resolving power is obtained as $R_{\mathrm{eff}} \sim (0.9/\langle\mathrm{DIMM}\rangle) \times R_{\mathrm{nom}}$ (see D'Odorico et al. 2022). Note, however, that these determinations have uncertainties of the order of 10% (see V. D'Odorico et al. 2023, in preparation).

2.1. Line Fitting

The analysis of the spectra has been carried out with the *Astrocook* software package. In *Astrocook*, absorption lines are detected as prominent local minima in the flux density spectrum, and then they are identified by cross-matching their wavelengths with a list of ionic transitions commonly observed in QSO spectra and finding coincidences among the obtained redshift values.

For our study, we need to identify absorption systems with H I column densities in the range $17.2 \leqslant \log(N_{\mathrm{H\,I}}/\mathrm{cm}^{-2}) \leqslant 20.3$, i.e., LLSs and sub-DLAs, which can trace diffuse gas, such as the one in the outskirts of galaxies and in cosmic filaments (Lofthouse et al. 2023). To this aim, we searched the XQ-100 spectra for singly ionized magnesium doublets, Mg II, which are good probes of the optically thick, low-ionization gas. Mg II is one of the best known examples of strong resonance-line doublets: it has rest-frame wavelengths (see Table 3) longer than H I Lyα (Lyα), and therefore it appears on the red side of the Lyα emission line in the QSO spectrum. For this reason, it is relatively easy to identify as it is not embedded in the thick Lyα forest. The search for Mg II doublets was carried out using an automatic recipe of the *Astrocook* software. Subsequently, the detection of the absorption lines was confirmed visually. In our analysis we have not made any attempt to reach or determine the completeness of the absorber sample since it was not relevant for our scientific purposes.

In each line of sight, we restricted our search to a redshift range that avoids the proximity region of the quasar (5000 km s^{-1} from the quasar emission redshift) and that allows us to cover the H I Lyα and Lyβ transitions of a given absorption system, for a more reliable determination of the H I column density. Furthermore, we have excluded the interval 13500–14500 Å affected by strong telluric lines. This wavelength range corresponds to the redshift range $z \simeq 3.83$–4.18 for Mg II λ2796.

Detected systems are then modeled with Voigt profiles in the context of *Astrocook*. The Voigt profile fitting provides the central line redshift, z, the column density, N, and the Doppler broadening parameter, b. After the identification of the Mg II doublets, we proceeded with the search of other low-ionization lines (see Table 3) at the same redshift. Assuming that they originate from the same gas and that turbulent motion is dominant over the thermal one, we fitted all with the same redshift components having the same Doppler parameters. On the other hand, C IV and Si IV absorption lines, if present, have generally a different velocity structure, and they were fitted separately. To better constrain the chemical properties of our absorbers, we also estimated column density upper limits, in particular for Fe II and O I if they were not detected. We used Equations (2) and (3) of D'Odorico et al. (2016) adapted for 1σ limits assuming a Doppler broadening parameter equal to one of the other low-ionization transitions in the system and the spectral velocity bin (UVB: 20 km s^{-1}; VIS: 11 km s^{-1}; NIR: 19 km s^{-1}) from López et al. (2016). The neutral hydrogen column density was determined by considering in the fit all the lines in the Lyman series free from strong blending.

A well-known issue related to absorption-line fitting is the identification of saturated lines. Indeed, with the resolving power provided by X-shooter, in many cases the lines are not resolved, and therefore it is difficult to understand when they are saturated. We adopted the following empirical procedure for metal lines: when the difference between the normalized flux and the depth of the line was >0.7, we assumed that the line was saturated and considered the determined column density as a lower limit. In this hypothesis we are neglecting the possible dependence on the Doppler parameter value.

We selected 51 Mg II absorption systems plus three previously identified LLS systems whose Mg II absorption falls in the telluric band (S. Cristiani 2023, private communication), for a total of 54 absorption systems. We compared our sample with those of prior studies of the XQ-100 survey investigating DLAs and sub-DLAs (Berg et al. 2016, 2017, 2019, 2021), finding matches for 17 DLAs and 16 sub-DLAs. We excluded the DLAs from our sample and used the H I column density determined in Berg et al. (2019) for the sub-DLAs. Our analysis was then focused on a sample of 16 sub-DLAs and 21 LLSs.

Three of the QSOs in our sample (J0247−0556, J1111−0804, and J1723+2243) have a reduced UVES spectrum available from the SQUAD database (Murphy et al. 2019). We verified with *Astrocook* that for our systems there is a good agreement between column densities measured in the X-shooter and UVES spectra.

2.2. Determination of Chemical Abundances

The gas in LLSs and sub-DLAs is not fully neutral; therefore, it is necessary to apply an ionization correction to translate the observed ionic column densities into element abundances and thus into gas metallicity.

To infer the chemical composition and the physical state of the absorbing gas, we have used ionization models based on

---

[13] https://github.com/DAS-OATs/astrocook

Table 1
Redshift Range within Which the Absorption Systems Were Searched

Quasar	z_{max}	z_{min}	*R* (UVB)	*R* (VIS)	*R* (NIR)	Quasar	z_{max}	z_{min}	*R* (UVB)	*R* (VIS)	*R* (NIR)
J0003−2603	4.125	3.339	5400	8900	5600	J1034+1102	4.290	3.478	6200	9200	5800
J0006−6208	4.440	3.807	5400	8900	5600	J1036−0343	4.531	3.682	7000	10400	6500
J0030−5129	4.173	3.379	5400	8900	5600	J1037+2135	3.634	2.923	5400	8900	5600
J0034+1639	4.292	3.723	5400	8900	5600	J1037+0704	4.141	3.352	5400	8900	5600
J0042−1020	3.882	3.133	7900	11800	7400	J1042+1957	3.636	2.925	5400	8900	5600
J0048−2442	4.083	3.303	7800	11600	7300	J1053+0103	3.674	2.957	5400	8900	5600
J0056−2808	3.635	3.086	5400	8900	5600	J1054+0215	3.973	3.210	7700	11400	7200
J0057−2643	3.661	2.946	6600	9800	6100	J1057+1910	4.137	3.349	8000	12000	7500
J0100−2708	3.546	2.849	5400	8900	5600	J1058+1245	4.341	3.522	5400	8900	5600
J0113−2803	4.314	3.499	7800	11600	7300	J1103+1004	3.595	2.890	5400	8900	5600
J0117+1552	4.243	3.622	5400	8900	5600	J1108+1209	3.672	3.095	6500	9700	6100
J0121+0347	4.125	3.339	5400	8900	5600	J1110+0244	4.158	3.367	6600	9800	6100
J0124+0044	3.840	3.098	5400	8900	5600	J1111−0804	3.922	3.291	9200	13600	8500
J0132+1341	4.152	3.553	6700	9900	6200	J1117+1311	3.629	2.919	5400	8900	5600
J0133+0400	4.185	3.563	8200	12100	7600	J1126−0126	3.617	2.909	5400	8900	5600
J0137−4224	3.971	3.208	5400	8900	5600	J1126−0124	3.737	3.072	5400	8900	5600
J0153−0011	4.206	3.407	5400	8900	5600	J1135+0842	3.847	3.100	5400	8900	5600
J0211+1107	3.973	3.210	7300	10800	6800	J1201+1206	3.522	3.040	9200	13600	8500
J0214−0518	3.985	3.221	6400	9500	6000	J1202−0054	3.593	2.889	5400	8900	5600
J0234−1806	4.305	3.689	5400	8900	5600	J1248+1304	3.709	2.986	5400	8900	5600
J0244−0134	4.055	3.439	8100	12100	7600	J1249−0159	3.655	3.039	5400	8900	5600
J0247−0556	4.234	3.600	5400	8900	5600	J1304+0239	3.618	2.910	5400	8900	5600
J0248+1802	4.439	3.604	8100	12100	7600	J1312+0841	3.735	3.009	7100	10500	6600
J0255+0048	4.003	3.387	7100	10500	6600	J1320−0523	3.717	2.993	6200	9200	5800
J0307−4945	4.716	3.896	7000	10400	6500	J1323+1405	4.067	3.316	6900	10300	6500
J0311−1722	4.034	3.262	6600	9800	6100	J1330−2522	3.949	3.190	7700	11400	7200
J0401−1711	4.227	3.669	8900	13100	8300	J1331+1015	3.845	3.102	7800	11600	7300
J0415−4357	4.073	3.510	6700	10000	6300	J1332+0052	3.507	2.942	5400	8900	5600
J0424−2209	4.329	3.762	5400	8900	5600	J1336+0243	3.810	3.072	7800	11600	7300
J0523−3345	4.385	3.559	8700	12900	8100	J1352+1303	3.693	2.973	5400	8900	5600
J0529−3526	4.418	3.787	6500	9600	6100	J1401+0244	4.418	3.718	8300	12300	7800
J0529−3552	4.172	3.538	7300	10800	6800	J1416+1811	3.602	2.896	5400	8900	5600
J0714−6455	4.465	3.872	10600	15700	9900	J1421−0643	3.688	2.978	5400	8900	5600
J0747+2739	4.133	3.389	5400	8900	5600	J1442+0920	3.529	2.834	6700	10000	6300
J0755+1345	3.674	2.957	5400	8900	5600	J1445+0958	3.562	2.862	7000	10400	6500
J0800+1920	3.947	3.420	5400	8900	5600	J1503+0419	3.664	2.948	5400	8900	5600
J0818+0958	3.694	3.041	7800	11600	7300	J1517+0511	3.559	2.860	5400	8900	5600
J0833+0959	3.713	2.990	6400	9400	5900	J1524+2123	3.592	2.981	5400	8900	5600
J0835+0650	3.990	3.430	7900	11800	7400	J1542+0955	3.992	3.226	7100	10500	6600
J0839+0318	4.234	3.596	6500	9600	6100	J1552+1005	3.715	3.179	7100	10500	6600
J0920+0725	3.636	2.925	6900	10300	6400	J1621−0042	3.710	2.987	5400	8900	5600
J0935+0022	3.739	3.012	5400	8900	5600	J1633+1411	4.379	3.686	7100	10500	6600
J0937+0828	3.703	2.981	7000	10300	6500	J1658−0739	3.750	3.193	5400	8900	5600
J0955−0130	4.418	3.618	6900	10300	6500	J1723+2243	4.531	3.815	5400	8900	5600
J0959+1312	4.064	3.385	5400	8900	5600	J2215−1611	3.995	3.372	10400	15400	9700
J1013+0650	3.790	3.055	9800	14600	9200	J2216−6714	4.479	3.725	6600	9800	6200
J1018+0548	3.514	2.914	7100	10500	6600	J2239−0552	4.557	3.704	5400	8900	5600
J1020+0922	3.655	2.941	7400	11000	6900	J2251−1227	4.157	3.678	10600	15700	9900
J1024+1819	3.525	2.831	6700	9900	6200	J2344+0342	4.248	3.443	7200	10700	6700
J1032+0927	4.003	3.288	7000	10400	6500	J2349−3712	4.219	3.567	6700	9900	6200

Note. Corrected resolving power for the three arms of each QSO (UVB, VIS, NIR).

radiative transfer calculations at equilibrium and for a single gas phase. These calculations are the input of a Bayesian formalism that exploits Markov Chain Monte Carlo (MCMC) techniques to derive the posterior probability distribution function for quantities of interest, such as the metallicity, Z, and the physical density, $n_{\rm H}$, of the absorbing gas. In particular, the MCMC method we have adopted (Fumagalli et al. 2016) uses a grid of CLOUDY models. CLOUDY (ver. 17; Ferland et al. 2017) is an open-source photoionization code that maps each set of input parameters into the corresponding column densities of all metal ions that we considered in this work. The MCMC sampler searches Z and $n_{\rm H}$ for models with the column density pattern that best matches the neutral hydrogen column density, $N_{\rm H\,I}$, and the metal ion column densities fitted by the software *Astrocook*. The output of the MCMC modeling is a probability distribution of the sets of parameters Z and $n_{\rm H}$. In this work, we adopt the minimal model parameters (Fumagalli et al. 2016), which assumes a slab of gas at constant density illuminated on one side by both the UV background (Haardt & Madau 2012) and the cosmic microwave background. All

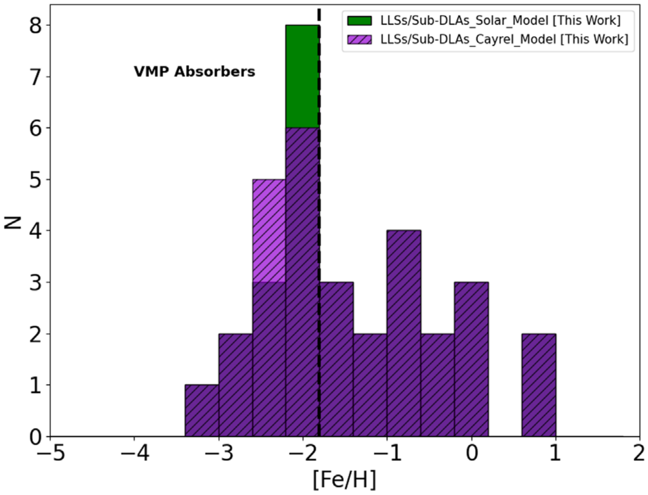

Figure 1. MDF of our 30 absorbers assuming solar relative abundances (green) and *Cayrel's* relative abundances (purple) in the photoionization model. A dashed line at $[\mathrm{Fe/H}] = -1.8$ separates the very metal-poor (VMP) absorbers from the others.

metals are assumed to be in the gas phase with a solar abundance pattern (Asplund et al. 2009).

To obtain the ionization corrections ion by ion, we run again the CLOUDY system by system optimizing the values of Z and n_{H} determined by the MCMC run based on the observed column densities. We vary the parameters in an interval corresponding to the 10th and 90th percentile of their posterior distribution function. We considered a narrow range because the optimization on the full parameter space had already been performed by the MCMC code. Finally, from the photoionization model we obtained the corrections for each ion of each element.

Once the column densities obtained from the Voigt fit have been corrected for ionization, we derived the absolute abundances of the various elements. The corrected column density of an element X has been determined using the formula $N(X) = N(X_i)/\mathrm{IC}(X_i)$, where $N(X_i)$ is the column density of the ion fitted from the spectrum and $\mathrm{IC}(X_i)$ is the ionization correction obtained from CLOUDY. Then, we derived the relative abundances of each element as

$$[X/\mathrm{H}] = \log\left(\frac{N_X}{N_{\mathrm{H}}}\right) - \log\left(\frac{N_X}{N_{\mathrm{H}}}\right)_{\odot}, \tag{1}$$

where N_{H} and N_X are respectively the column density of hydrogen and of a specific element X and $\log(N_X/N_{\mathrm{H}})_{\odot}$ is the solar abundance (Asplund et al. 2009).

In Figure 1, we show the metallicity distribution function (MDF) derived for our absorbers, i.e., the number of systems in different bins of [Fe/H], assuming solar relative abundances in the photoionization model (solar model). Note that we restricted our analysis only to the 30 absorbers for which we could determine a measure/upper limit of Fe II (with respect to the 37 previously selected LLSs and sub-DLAs). Furthermore, we are here assuming that all our [Fe/H] values are measurements, although for 10 absorbers (5 if we consider those very metal-poor) we only have upper limits on Fe II (see Figure 5).

The MDF is characterized by a pronounced peak at $[\mathrm{Fe/H}] \sim -2$ and extends over a broad range in [Fe/H], at both higher and lower values. In particular, there are 14 very metal-poor absorption systems with $[\mathrm{Fe/H}] < -2$, where we include also those systems for which $[\mathrm{Fe/H}] - 1\sigma < -2$. We have verified that these $[\mathrm{Fe/H}] < -2$ systems are also characterized by a low total metallicity with respect to the solar value (see Figure 6 and Table 2) and therefore that they are not just iron-poor because of dust depletion. On the other hand, the shape of the MDF at $[\mathrm{Fe/H}] > -2$ is less constrained owing to the fact that the iron measurements could be affected by dust depletion: the effect would be to increase the value of [Fe/H].

Note that the chemical abundance pattern of very metal-poor stars, at $[\mathrm{Fe/H}] < -2$, is well established to be different from the solar value (e.g., Cayrel et al. 2004; Bonifacio et al. 2009; Yong et al. 2013). For this reason, we recompute the ionization corrections for our very metal-poor absorbers by assuming the chemical abundance pattern derived by Cayrel et al. (2004) for a sample of C-normal giant stars with $-4 < [\mathrm{Fe/H}] < -2$ in the MW halo (hereafter we will refer to this pattern as *Cayrel*). This average chemical abundance pattern is indeed characterized by a very small star-to-star scatter. Hence, it can be considered as a "reference" for very metal-poor environments.

Table 4 reports the values assumed in the new CLOUDY models, which are those derived by Cayrel et al. (2004) corrected for 3D and/or Non-Local Thermodynamical Equilibrium (NLTE) effects and for stellar physical processes that can alter the measured abundances. These corrections are required to use the stellar abundance values for the gaseous component.

In particular, we adopted (i) the [C/Fe] value derived for dwarfs (Bonifacio et al. 2009), since the photospheric carbon abundances in giant stars can be altered by convective mixing—in other words, we assumed that the difference between giant and dwarfs is due to the first dredge-up; (ii) the original [O/Fe] value derived by Cayrel et al. (2004), since Bonifacio et al. (2009) demonstrated that in giant stars 3D effects for oxygen are not important; (iii) the magnesium value derived by Andrievsky et al. (2010) in order to account for NLTE effects; and (iv) the [Al/Fe] and [Si/Fe] values reported by Cayrel et al. (2004), since aluminum was already corrected for NLTE effects and NLTE effects for silicon are expected to be very weak.

We defined a modified χ^2 to establish which model (solar or *Cayrel*) reproduces better our observed column densities, $\chi^2 = (\sum_i((N^i_{\mathrm{model}} - N^i_{\mathrm{obs}})/\sigma)^2)^{1/2}$, where N_{model} and N_{obs} are the modeled and observed ionic column density values, respectively, and σ is the relative error in the observed value. More than 75% (11/14) of the very metal-poor absorbers are better modeled with *Cayrel*'s abundance pattern than with solar (see Table 5).

The observed column densities are better reproduced for most of the ions. In addition, the relative abundances obtained with the new photoionization model are consistent with the abundances obtained with the solar model for most chemical elements.

The results of the Voigt profile fitting for the 14 very metal-poor absorption systems are available online as supplemental material. The tables reporting the fit parameters are available for *all* 37 absorption systems.[14]

---

[14] Note that for the 16 absorbers with $[\mathrm{Fe/H}] > -2$ and for the 7 without iron detection (or upper limits), we fit each ionic transition (or multiplet) independently. We only refined the analysis for the 14 very metal-poor absorption systems, $[\mathrm{Fe/H}] < -2$, being the main focus of the work.

Table 2

Absorption Redshift, Neutral Hydrogen Column Density, Iron Abundance, and Relative Chemical Abundances for All Absorption Systems with a Measure/Upper Limit of Fe II (30)

Quasar	$z_{\rm abs}$	$N_{\rm H\,I}$	$\log(Z/Z_\odot)$	[Fe/H]	[C/H]	[O/H]	[Mg/H]	[Al/H]	[Si/H]	[C/Fe][a]
J0042−1020	3.62953	18.6 ± 0.3	−1.55	−1.3 ± 0.3	>−1.1	−1.6 ± 0.3	−1.1 ± 0.3	−1.8 ± 0.3	−1.2 ± 0.3	>+0.11
J0056−2808	3.58045	17.4 ± 0.2	−0.97	+0.70 ± 0.19	>+2.1	+1.7 ± 0.2	>+0.3	−0.6 ± 0.3	+0.1 ± 0.2	>+1.41
J0124+0347	3.67488	17.9 ± 0.2	−1.98	<−0.96	−2.46 ± 0.18		−1.84 ± 0.17	−2.8 ± 0.2	−2.07 ± 0.17	>−1.50
J0133+0400	3.99668	17.4 ± 0.2	−1.85	+0.8 ± 0.2	−0.8 ± 0.2	+2.2 ± 0.2		−1.6 ± 0.2	−0.5 ± 0.2	−1.59 ± 0.16
J0211+1107[b]	3.50250	19.9 ± 0.2	−1.69	−2.0 ± 0.2	−1.3 ± 0.2		−1.7 ± 0.2	−1.5 ± 0.2	−0.9 ± 0.2	+0.66 ± 0.12
J0234−1806	4.22817	19.2 ± 0.2	−1.06	−0.9 ± 0.2	>+0.5	−0.5 ± 0.2	>−0.7	−0.9 ± 0.2	−0.4 ± 0.3	>+1.54
J0247−0556[b]	4.13952	18.9 ± 0.2	−2.26	−2.0 ± 0.2	−1.6 ± 0.2	−1.1 ± 0.2		−2.6 ± 0.2	−1.7 ± 0.2	+0.43 ± 0.11
J0307−4945	4.21345	17.2 ± 0.2	−1.49	<−0.82	>+1.0		−0.8 ± 0.2	−1.6 ± 0.2	−0.5 ± 0.2	>+1.89
J0529−3552	4.06561	18.6 ± 0.2	−2.00	−1.6 ± 0.2	−1.4 ± 0.2	−1.2 ± 0.2		−2.4 ± 0.2	−1.4 ± 0.2	+0.2 ± 0.3
J0800+1920[b]	3.42856	19.9 ± 0.2	−2.85	−3.0 ± 0.2	−2.3 ± 0.2		−2.2 ± 0.2	−2.9 ± 0.2	−2.3 ± 0.2	+0.65 ± 0.09
J0818+0958[b]	3.45615	18.8 ± 0.2	−2.51	−2.0 ± 0.2	−2.1 ± 0.2	<−2.3	−1.9 ± 0.2	−2.4 ± 0.2	−2.0 ± 0.2	−0.04 ± 0.09
J0818+0958	3.53141	18.0 ± 0.2	−2.30	<+0.07	−2.09 ± 0.16		−1.79 ± 0.16	−2.08 ± 0.16	−2.34 ± 0.16	>−2.17
J0835+0650[b]	3.51256	18.7 ± 0.2	−2.49	<−2.59	−1.9 ± 0.2		−1.9 ± 0.2	−2.5 ± 0.2	−2.1 ± 0.2	>+0.69
J1013+0650	3.23534	17.3 ± 0.2	−1.49	<−0.5	>−1.1		−1.1 ± 0.2	−1.8 ± 0.2	−1.2 ± 0.2	>−0.56
J1018+0548[b]	3.38500	19.3 ± 0.2	−2.52	−2.3 ± 0.2	−2.1 ± 0.2	−1.5 ± 0.2	−1.9 ± 0.2	−3.2 ± 0.2	−2.1 ± 0.2	+0.20 ± 0.13
J1111−0804[b]	3.48170	19.9 ± 0.2	−2.22	−1.91 ± 0.16	−1.72 ± 0.16	−1.51 ± 0.16	−1.65 ± 0.16	−2.24 ± 0.15	−1.75 ± 0.15	+0.19 ± 0.08
J1111−0804[b]	3.75837	18.6 ± 0.2	−2.42	<−2.91	−2.1 ± 0.2	<−2.5	−2.0 ± 0.2	−2.4 ± 0.2	−2.1 ± 0.2	>+0.78
J1117+1311	3.27522	17.9 ± 0.2	−1.93	<−0.92	−0.64 ± 0.16		−1.45 ± 0.18	−2.01 ± 0.14	−1.77 ± 0.15	>+0.29
J1117+1311[b]	3.43372	18.7 ± 0.2	−2.91	<−2.47	−2.55 ± 0.15	<−1.9	−2.13 ± 0.18	−3.08 ± 0.14	−2.4 ± 0.2	>−0.07
J1249−0159	3.10265	17.70 ± 0.15	−1.06	−0.26 ± 0.13	−0.68 ± 0.13		>−0.82	−1.18 ± 0.13	−0.79 ± 0.13	−0.42 ± 0.08
J1304+0239	3.21072	18.30 ± 0.15	−1.41	−0.11 ± 0.13	>+1.73		>+0.96	−0.09 ± 0.18	0.04 ± 0.13	>+1.86
J1332+0052[b]	3.42107	18.5 ± 0.2	−2.48	−2.0 ± 0.2	−2.0 ± 0.2		−2.2 ± 0.2	−2.8 ± 0.2	−2.0 ± 0.2	−0.06 ± 0.09
J1352+1303	3.00680	18.80 ± 0.15	−0.99	−1.27 ± 0.13	−1.26 ± 0.13		>−0.5	−1.15 ± 0.13	−1.16 ± 0.13	0.00 ± 0.07
J1542+0955	3.28223	17.30 ± 0.15	−0.25	−0.08 ± 0.12	+0.19 ± 0.17		>−0.42	−0.26 ± 0.11	−0.34 ± 0.12	+0.28 ± 0.15
J1552+1005[b]	3.44250	19.0 ± 0.2	−2.70	−2.2 ± 0.2	−2.0 ± 0.2	−1.9 ± 0.2	−2.2 ± 0.2	−2.9 ± 0.2	−2.2 ± 0.2	+0.17 ± 0.16
J1621−0042	3.10570	19.60 ± 0.15	−1.43	−1.41 ± 0.16	−1.26 ± 0.16		>+0.1	−1.39 ± 0.16	−0.99 ± 0.16	+0.16 ± 0.07
J1658−0739[b]	3.54604	19.0 ± 0.2	−2.88	<−3.30	−1.9 ± 0.2		−2.11 ± 0.14		−2.51 ± 0.13	>+1.41
J1658−0739[b]	3.69551	18.5 ± 0.2	−2.83	<−2.36	−2.3 ± 0.2	<−1.9	−2.52 ± 0.16		−2.51 ± 0.19	>+0.10
J1723+2243[b]	4.24710	18.8 ± 0.2	−2.57	−1.9 ± 0.2	−1.93 ± 0.17	−1.63 ± 0.16	−1.91 ± 0.17	−2.49 ± 0.16	−2.07 ± 0.17	−0.01 ± 0.10
J2215−1611	3.70140	19.20 ± 0.15	−1.75	−1.46 ± 0.16	>−1.47	−1.29 ± 0.16	>−1.43	−1.97 ± 0.16	−1.34 ± 0.19	>0.00

Notes.

[a] [C/Fe] is computed directly by using the carbon and iron column densities.

[b] Very metal-poor absorption systems with [Fe/H] < −2. The carbon-enhanced very metal-poor absorbers are shown in bold.

Table 3
Ionic Transitions Considered in Our Study and Their Rest-frame Wavelength

Ion	λ (Å)
H I Lyα	1215.6701
H I Lyβ	1025.7223
Mg II	2796.35, 2803.53
Fe II	1608.45, 2344.21, 2382.77, 2586.65, 2600.17
Si II	1260.42, 1304.37, 1526.71, 1808.01
O I	1302.17
C II	1334.53
Al II	1670.79
Al III	1854.72, 1862.79
Zn II	2026.137, 2062.66
C IV	1548.20, 1550.78
Si IV	1393.76, 1402.77

Table 4
Average Abundance Ratios, [X/Fe], for the Sample of Very Metal-poor Giant Stars in the MW Halo Studied by Cayrel et al. (2004) and Corrected to Account for Internal Mixing along with NLTE Effects (See Text)

Element	[X/Fe]
C	+0.45
O	+0.67
Mg	+0.61
Al	−0.10
Si	+0.44

Table 5
Modified χ^2 Parameter That Estimates the Agreement between the Observed Column Densities of a Given Chemical Ion and the Column Densities Computed by the Model

Quasar	$z_{\rm abs}$	$\chi^2_{\rm Solar}$	$\chi^2_{\rm Cayrel}$
J0211+1107	3.50250	9	19
J0247−0556	4.13952	34	16
J0800+1920	3.42856	67	7
J0818+0958	3.45615	178	10
J0835+0650	3.51256	14	7
J1018+0548	3.38500	32	8
J1111−0804	3.48170	27	21
J1111−0804	3.75837	13	38
J1117+1311	3.43372	15	14
J1332+0052	3.42107	32	31
J1552+1005	3.44250	33	9
J1658−0739	3.54604	38	24
J1658−0739	3.69551	16	19
J1723+2243	4.24710	19	13

Note. We report the value for all the very metal-poor absorbers.

An example figure of two very metal-poor absorption systems is shown in the Appendix together with a portion of the fit parameters table for guidance.

3. Results

3.1. Metallicity Distribution Function

Figure 1 shows the new MDF obtained for our absorbers, adopting the *Cayrel* abundances for very metal-poor systems and the solar values for those with [Fe/H] > −2. We can first note that the shape of the MDF remains essentially unvaried with respect to the one that was obtained by assuming solar values for all absorbers. This is because most of the changes are small, with an [Fe/H] difference <0.4 dex, i.e., smaller than the width of the MDF bin. By further inspecting Figure 1, we see that the MDF of our gaseous absorbers is roughly bimodal: the first broad peak is around [Fe/H] ∼ −0.8, while the second one, which is more pronounced, appears at [Fe/H] ∼ −2. This result implies that these absorbers are likely a variegated population (e.g., Fumagalli et al. 2016).

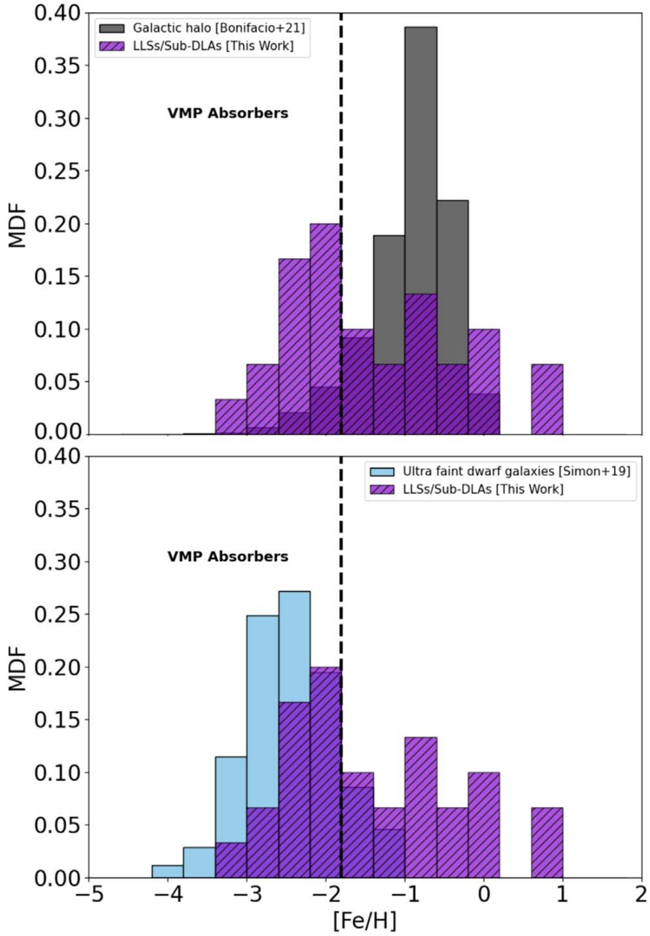

Figure 2. Comparison between the MDFs of our 30 absorbers, assuming *Cayrel's* relative abundances in the photoionization model, and the MDF of ∼140,000 stars in the Galactic halo (Bonifacio et al. 2021; top panel) and of 350 stars in 26 UFDs (Simon 2019; bottom panel). A dashed line at [Fe/H] = −1.8 separates the very metal-poor (VMP) absorbers from the others.

We compare the normalized MDF of our high-redshift absorption systems (*Cayrel* model) with those of ancient very metal-poor stars observed in the Galactic halo (Bonifacio et al. 2021) and in Local Group ultrafaint dwarf galaxies (UFDs; Simon 2019), respectively, in the top and bottom panels of Figure 2. We are aware that we are comparing the chemical abundances of diffuse high-redshift gas, which can be located in the outskirts of galaxies, with the ones of ancient local stars. Still, the main point behind our comparison is that stars are born from gas.

The MDF of our sample spans a wide range of [Fe/H], covering the values measured in stars of both the MW stellar halo and nearby UFDs. The distribution of the halo stars covers a similar range of [Fe/H] with respect to our absorbers, but it has a different shape. Indeed, the stars of the Galactic halo have

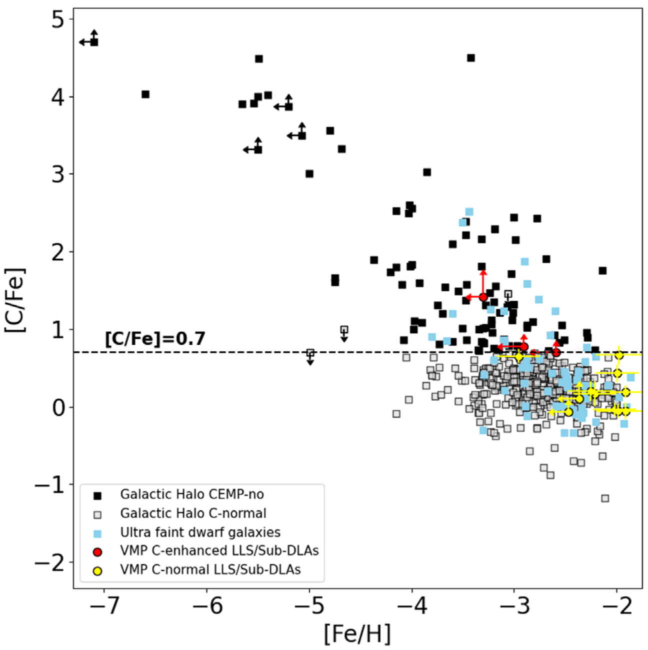

Figure 3. Comparison between the carbon-to-iron ratio of the gaseous absorption systems at different [Fe/H] and the very metal-poor compilation of stars in UFDs (light-blue squares) and the Galactic halo. CEMP-no halo stars are shown as black squares, C-normal halo stars as gray squares. Stellar measurements have typical 1σ errors of 0.2 dex. Red and yellow circles are C-enhanced and C-normal very metal-poor absorbers, respectively, which include LLSs and sub-DLAs.

a unique peak, which is more pronounced and appears around $[\mathrm{Fe/H}] \sim -1$. Note that, although very rare and hence almost invisible in the normalized MDF, stars with $[\mathrm{Fe/H}] < -2.5$ in the Galactic halo are those showing the chemical imprint of the first stars (see Figure 4). The low-Fe peak of our absorbers, therefore, suggests similarities between these high-z absorbers and the gas that may have hosted the imprint of the first stars, like the birth environment of very metal-poor halo stars.

The MDF of UFDs covers a narrower range of iron abundances, $-4 < [\mathrm{Fe/H}] < -1$, than the MDF of our absorption systems and shows a peak at $[\mathrm{Fe/H}] = -2.5$, almost overlapping with the low-Fe peak of the MDF of our absorbers (Figure 2, bottom panel). These findings suggest that our absorption systems might represent the gas-rich counterpart of UFDs at high redshift (Salvadori & Ferrara 2012; Skúladóttir et al. 2018). The absence of ultrametal-poor absorption systems ($[\mathrm{Fe/H}] < -4$), which are observed among Galactic halo stars, could be due to observational biases. On the one hand, we select our systems by the presence of the singly ionized magnesium doublet; on the other hand, the resolution and S/N of the XQ-100 spectra do not allow us to put very stringent upper limits on the iron column density, when the ionic lines are not detected.

3.2. Carbon-enhanced Systems: Stellar Relics versus High-z Absorbers

In Figure 3 we compare the carbon-to-iron ratio, [C/Fe], measured in our very metal-poor gaseous systems and in Local Group stars (halo and UFDs) as a function of [Fe/H]. The stellar data we used were taken from Salvadori et al. (2015) and updated with new measurements for stars in UFDs (Ji et al. 2016; Spite et al. 2018) and newly discovered extremely metal-poor stars in the MW (Bonifacio et al. 2018; François et al. 2018; Starkenburg et al. 2018; Aguado et al. 2019; González Hernández et al. 2020). All [C/Fe] values are corrected to account for internal mixing processes (Placco et al. 2014). We see that our very metal-poor absorbers exhibit the same trend in [C/Fe] versus [Fe/H] that is observed in Local Group stars, i.e., an increasing [C/Fe] value for decreasing [Fe/H]. In particular, we see a nice overlapping in the [C/Fe] and [Fe/H] values of our absorbers and of stars in UFDs. This suggests an additional link between the ISM of UFDs at the time of formation of their stellar populations and our gas-rich absorbers.

We also notice that among the 14 very metal-poor absorbers, 3 are carbon-enhanced, with $[\mathrm{C/Fe}] > +0.7$. These C-enhanced absorbers have an upper limit on Fe II, implying that their true [C/Fe] could be even larger. Note that there are two other absorption systems with $[\mathrm{C/Fe}] \approx +0.7$. Still, since the definition of C-enhanced very metal-poor absorbers varies in the literature, e.g., $[\mathrm{C/Fe}] \geqslant +0.7$ (e.g., Beers & Christlieb 2005) and $[\mathrm{C/Fe}] \geqslant +1.0$ (Bonifacio et al. 2015), we decided to include them in the C-normal subsample. For the three carbon-enhanced systems we checked the reliability of the column density measurements against our hypothesis of turbulent broadening with respect to thermal broadening. To this end, we fit the detected lines (Si II, C II, and Al II) assuming that they arise in the same gas and they are thermally broadened, and we find negligible variation of the column density ($\leqslant 0.02$) for all the transitions and $\leqslant 0.1$ for the C II in J1658−0739 at $z = 3.54604$.

In Figure 4 (top left panel) we show the [C/Fe] abundance as a function of [Fe/H] for *all* our absorption systems, i.e., including those at $[\mathrm{Fe/H}] > -2$, some of which are also C-enhanced. To make a full and detailed comparison with the stellar chemical abundances, we show in the same figure the [C/Fe] versus [Fe/H] values for *all* the observed stars in the MW and nearby dwarf galaxies (both UFDs and dwarf spheroidal), including also CEMP-*s* stars (Salvadori et al. 2015; Placco et al. 2019).

When considering this complete stellar sample, the excellent agreement between the chemical abundances measured in stars and gaseous absorbers at $[\mathrm{Fe/H}] < -2$ is even more evident, for both C-enhanced and C-normal systems. In particular, we see that very metal-poor C-enhanced absorbers never overlap with CEMP-*s* stars, which are shifted toward higher [Fe/H] at any given carbon-to-iron ratio. Conversely, we notice that systems with $[\mathrm{Fe/H}] > -2$ cover a wider range of [C/Fe] abundances than what is observed both in very metal-poor absorbers and in stars at the same [Fe/H]. Among these $[\mathrm{Fe/H}] > -2$ absorbers, we observe four C-enhanced systems, three of which nicely overlap with CEMP-*s* stars. We also see many (nine) C-normal absorbers that reside in the same region of C-normal stars. At $[\mathrm{Fe/H}] > 0$, where a few star measurements are available, we notice one C-enhanced absorber and two systems that are strongly C-deficient with respect to stars ($[\mathrm{C/Fe}] < -1$). The large [C/Fe] scatter of the absorbers in this $[\mathrm{Fe/H}] \geqslant -1$ regime, along with the presence of C-deficient systems, suggests that a nonnegligible amount of carbon (and iron) is likely depleted onto dust grains. Ultimately our results, which are in line with previous studies (e.g., Vladilo 1998; Quiret et al. 2016; De Cia et al. 2018; Vladilo et al. 2018), confirm that the dust contribution makes the comparison between the chemical abundances of gas and stars challenging at $[\mathrm{Fe/H}] \geqslant -1$, while it can be neglected in the very metal-

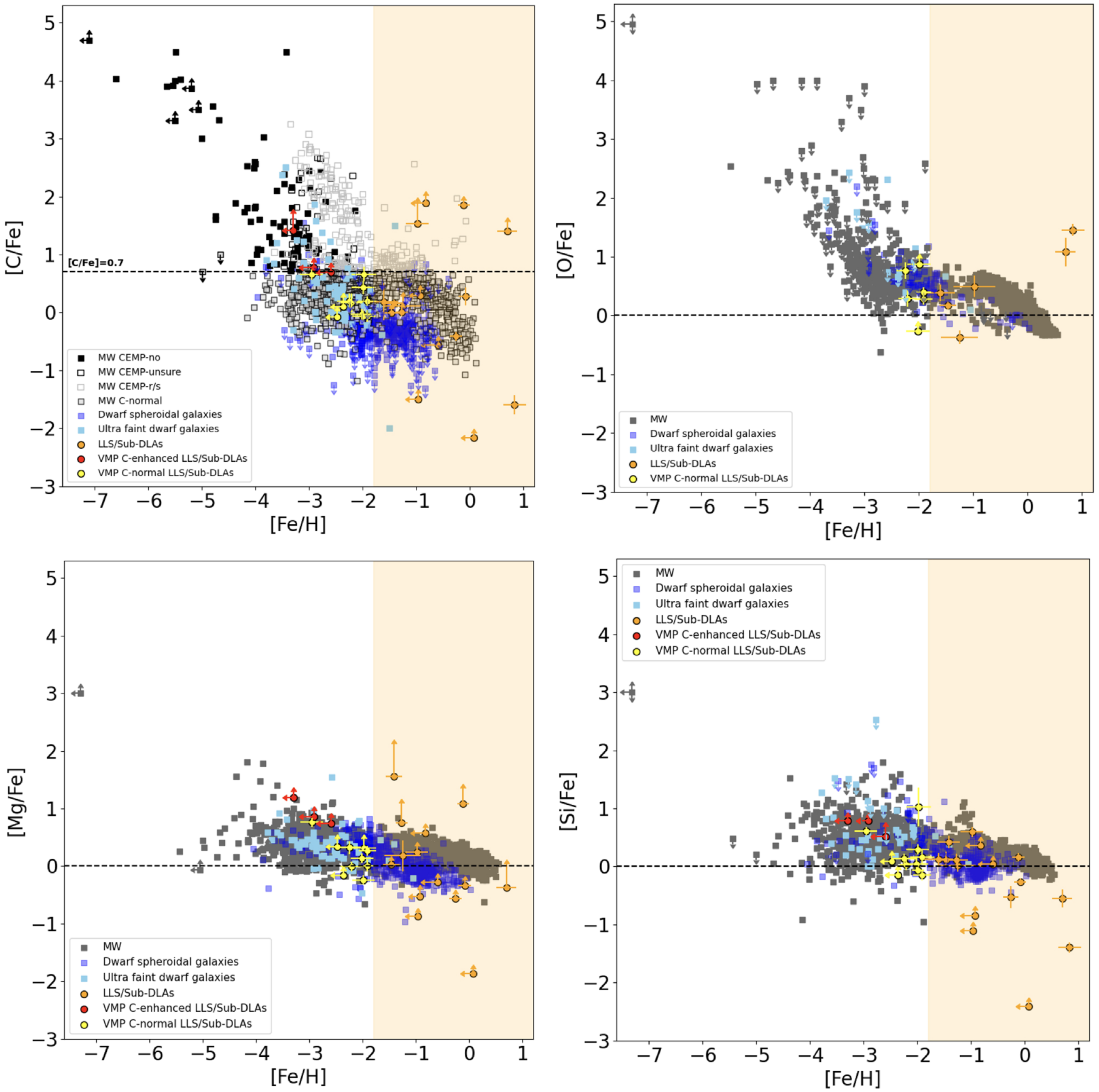

Figure 4. Top left panel: carbon-to-iron ratio as a function of [Fe/H] of all our gaseous absorption systems (filled circles) and of stars in UFDs (light-blue squares), dwarf spheroidal galaxies (blue squares), and the MW (gray/black squares). CEMP-no halo stars are shown as filled black symbols, C-normal halo stars as filled bordered light-gray squares, and CEMP-s/r stars as open symbols. Stellar measurements have typical 1σ errors of 0.2 dex. We distinguish among C-enhanced (red) and C-normal (yellow) very metal-poor absorbers. Orange circles are iron-rich absorbers. Other panels: comparison between the chemical abundances of the very metal-poor gaseous absorption systems (circles) and of the stars (squares) in the MW (gray), UFDs (light blue), and dwarf spheroidal galaxies (blue). Red and yellow circles are C-enhanced and C-normal very metal-poor absorbers, respectively. Orange circles are iron-rich absorbers. Stellar data are taken from the SAGA database (Suda et al. 2008). In all the panels the orange shaded area identifies the region where chemical abundances could be affected by dust depletion.

poor regime. Armed with these new findings, we can make further comparison between the chemical abundances of gas and stars in the very metal-poor regime.

3.3. Other Chemical Elements

To investigate more deeply the chemical enrichment history of our C-enhanced very metal-poor absorbers, in Figure 4 we compare the relative abundances of oxygen, magnesium, and silicon with respect to iron with those of ancient very metal-poor stars. The stellar data we used for these elements were taken from the SAGA database (Suda et al. 2008). The sample of stars is different from the one used for the carbon-to-iron ratio (Figure 3 and top left panel of Figure 4). For this reason we do not distinguish between CEMP-no and CEMP-s/r stars.

In Figure 4 we see that there is a general agreement between the chemical abundances of our absorption systems and the abundances of the stars in the MW and dwarf galaxies. Furthermore, at $[Fe/H] < -2$, we note the same trend for all the chemical elements in both stars and gas: the relative abundances increase as the [Fe/H] decreases. In particular, we see that C-enhanced very metal-poor absorbers are always overabundant also in the other chemical elements. The same is observed in CEMP-no stars (I. Vanni et al. 2023, in preparation).

Oxygen (Figure 4, top right panel) shows a similar trend to that of carbon even if we have fewer measurements. Indeed, we could measure the oxygen abundance only for 15 of the 30 systems for which we have the C abundance. In Figure 4, however, we report only 12 measurements since for three absorbers we have upper limits for both iron and oxygen. For the remaining systems, the O I absorption lines fall in the Lyα forest and are heavily blended with other absorption lines.

Magnesium (Figure 4, bottom left panel), which is produced by massive stars and released in the gas during SN explosions, shows a similar trend with iron to that seen for [C/Fe], although the values are less extreme. In particular, we see that all our C-enhanced very metal-poor systems are rich in magnesium, $[\mathrm{Mg/Fe}] > +0.7$, as observed in CEMP-no stars (e.g., Frebel et al. 2005; Keller et al. 2014; I. Vanni et al. 2023, in preparation, for a global view). The correlation between C and Mg tells us that these elements are probably produced by the same sources, i.e., most likely primordial low-energy SNe. At higher iron abundances, $[\mathrm{Fe/H}] > -2$, we see a large scatter.

Silicon (Figure 4, bottom right panel) also shows increasing relative abundances with respect to iron as [Fe/H] decreases. Once again, the C-enhanced very metal-poor systems are also enhanced in silicon, showing supersolar abundances. Also for silicon, we see that the system-to-system scatter increases at $[\mathrm{Fe/H}] > -2$, with abundance ratios spanning a wide range of values, many also in the subsolar regime. This result suggests that silicon is likely one of the chemical elements that is most affected by dust depletion.

We recall that the chemical abundances measured in stars might suffer NLTE effects, whose precise estimate, at the moment, is only available at $[\mathrm{Fe/H}] < -2$ for a small stellar subsample and for a few elements. Such effects can lower the [C/Fe] and [O/Fe] values measured in metal-poor stars by more than 0.3 dex (Amarsi et al. 2019), while they can increase the [Mg/Fe] value by +0.4 dex (Andrievsky et al. 2010), thus resulting in a better agreement between our C-enhanced very metal-poor absorbers and CEMP-no stars (see Figure 4). For [Al/Fe] the correction is extremely high, +0.65 dex (Cayrel et al. 2004), and for this reason we decided not to make the comparison with the values measured in our absorbers.

Ultimately, Figure 4 demonstrates that in the very metal-poor regime, $[\mathrm{Fe/H}] < -2$, the chemical abundance ratios measured in our gaseous absorbers are in very good agreement with those of present-day stars and that our C-enhanced very metal-poor absorption systems reside in the same regions of CEMP-no stars and have the same chemical properties.

3.4. First-star Signatures

The results described in the previous sections emphasize the idea that our C-enhanced very metal-poor absorbers are the gaseous analogs of CEMP-no stars, which have been likely imprinted by primordial low-energy SNe. Indeed, in our absorption systems we see an overabundance of Mg and Si, which is also observed in CEMP-no stars. Magnesium and silicon are key elements since they are produced by primordial low-energy SNe but not by AGB stars, which are the pollutant of CEMP-*s* stars. AGB stars yield high C, N, and O and also produce Ba via the slow neutron-capture process.

In CEMP-*s* stars the C and Ba excess is expected to be acquired via mass transfer from a binary AGB companion, while in CEMP-no stars it is expected to be representative of the environment of formation. For this reason barium is used to discriminate between CEMP-*s* stars ($[\mathrm{C/Fe}] > +0.7$, $[\mathrm{Ba/Fe}] > +1.0$) and CEMP-no stars ($[\mathrm{C/Fe}] > +0.7$, $[\mathrm{Ba/Fe}] < 0.0$; e.g., Beers & Christlieb 2005). Unfortunately, no barium measurements are (nor will be) available for our absorption systems. Thus, to further validate the link between our C-enhanced very metal-poor absorbers and CEMP-no stars, we need to carry out additional tests.

In stellar archeology, the absolute abundance of carbon, $A(\mathrm{C})$, displayed as a function of [Fe/H], is used to discriminate among CEMP-no and CEMP-*s* stars when barium abundances are not available. Indeed, it has been shown (e.g., Spite et al. 2013; Bonifacio et al. 2015; Yoon et al. 2016) that these two different populations dwell in two well-separated regions: the high carbon band, $A(\mathrm{C}) > 7.4$, and the low carbon band, $A(\mathrm{C}) < 7.4$. The stars belonging to the low carbon band are mostly CEMP-no stars,[15] while those of the high carbon band are CEMP-*s* stars. We can thus use this diagnostic to unveil the nature of our C-enhanced absorption systems.

In Figure 5 we display the absolute carbon abundance of Local Group stars and of our absorbers as a function of [Fe/H]. For the absorption systems we computed $A(\mathrm{C}) = \log(N_{\mathrm{C}}/N_{\mathrm{H}}) + 12$, where N_{C} and N_{H} are the measured column densities corrected for ionization. We see that our three carbon-enhanced very metal-poor absorbers are found in the low C-band, which is consistent with what is found for CEMP-no stars. These systems are clearly separated from the C-enhanced absorbers at $[\mathrm{Fe/H}] > -2$, which populate the high carbon band where CEMP-*s* stars reside. In other words, the division between the low- and high-C band corresponds to a division in [Fe/H] of our C-enhanced absorbers. Hence, despite the lack of barium measurements, we can conclude that our three C-enhanced absorbers at $[\mathrm{Fe/H}] < -2$ are CEMP-no absorption systems, while the four at $[\mathrm{Fe/H}] > -2$ are CEMP-*s*. Note that the C-enhanced absorber recently discovered by Zou et al. (2020) resides in the CEMP-*s* region ($[\mathrm{Fe/H}] = -1.6$, $A(\mathrm{C}) = 9.0$). Thus, like for our four CEMP-*s* absorbers, the C-excess of the absorption system studied by Zou et al. (2020) most likely arises from the contribution of AGB stars and not from the chemical elements yielded by the first stars.

4. Discussion

All gathered evidence supports the idea that the newly discovered C-enhanced very metal-poor absorption systems are the gaseous $z \sim 3$–4 analogs of present-day CEMP-no stars. Hence, we propose to define *CEMP-no absorbers*, LLSs/sub-DLAs with $[\mathrm{Fe/H}] < -2$ and $[\mathrm{C/Fe}] > +0.7$. An increasing number of theoretical studies are supporting the idea that CEMP-no stars observed in different environments have been most likely enriched by the first stellar generations (e.g., Iwamoto et al. 2005; Salvadori et al. 2015; Liu et al. 2021).

---

[15] Stars belonging to the low carbon band can be subsequently divided into *Group II* and *Group III*, which might have different astrophysical origins (e.g., Yoon et al. 2016, 2019; Zepeda et al. 2022) possibly linked with various dust composition in Population III SN ejecta (e.g., Chiaki et al. 2017). However, given the upper limit on [Fe/H] of our CEMP-no absorbers, we are not able to distinguish between the two groups.

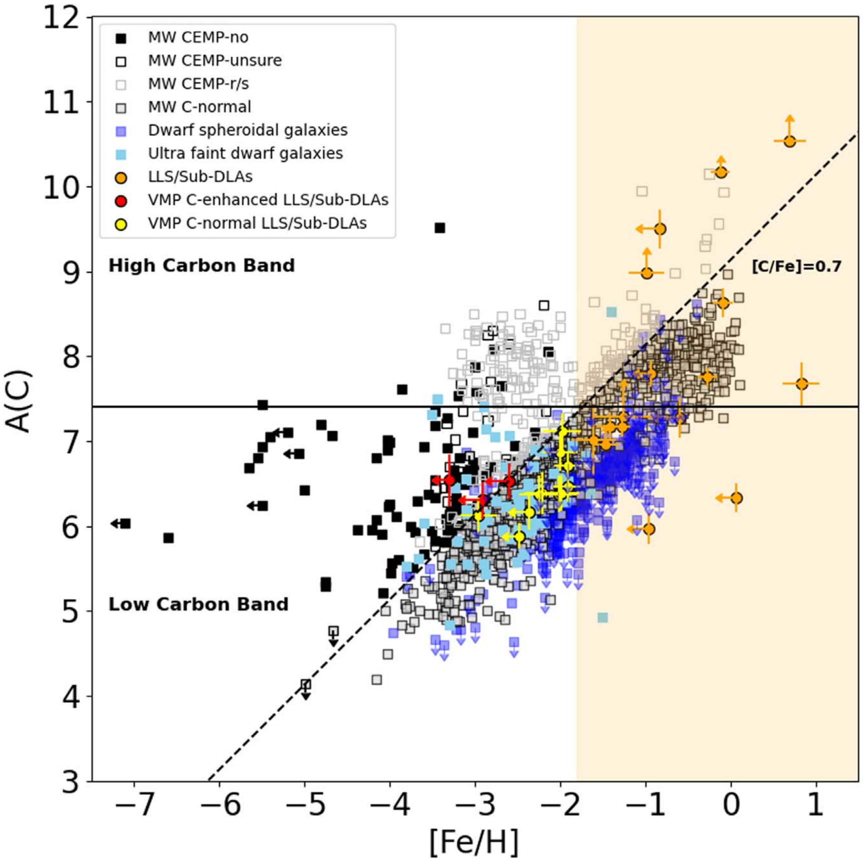

Figure 5. Absolute carbon abundance (A(C)) as a function of [Fe/H] of all our gaseous absorption systems (filled circles) and of stars in UFDs (light-blue squares), dwarf spheroidal galaxies (blue squares), and the MW (gray/black squares). CEMP-no halo stars are shown as filled black symbols, C-normal halo stars as filled bordered light-gray squares, and CEMP-s/r stars as open symbols. We distinguish among C-enhanced (red) and C-normal (yellow) very metal-poor absorbers. Orange circles are iron-rich absorbers. Stellar measurements have typical 1σ errors of 0.2 dex. We used the same stellar sample of Figure 4 (top left panel). The horizontal line separates the low-C band from the high-C band, while the dashed one indicates the value [C/Fe] = +0.7. The orange shaded area identifies the region where chemical abundances could be affected by dust depletion.

Thus, we are providing the first clues of gas enriched by Population III stars in high-z absorbers. Still, two questions naturally arise: what is the nature of these high-z CEMP-no absorption systems, and why have CEMP-no absorbers so far escaped detection?

4.1. Origin of CEMP-no Absorbers

Different semianalytical models and cosmological simulations have investigated the origin of CEMP-no stars in the Galactic halo (e.g., de Bennassuti et al. 2017; Hartwig et al. 2018; Liu et al. 2021) and in UFDs (e.g., Salvadori et al. 2015; Jeon et al. 2021; M. Rossi et al. 2023, in preparation). We can thus exploit these findings to interpret the properties of our CEMP-no absorption systems. The moderately high [C/Fe] and relatively high [Fe/H] values of CEMP-no absorbers can be explained as the result of two different enrichment mechanisms (I. Vanni et al. 2023, in preparation). These mechanisms are (i) a pollution solely driven by Population III stars, which explode as low-energy SNe with different masses (Hartwig et al. 2018; Jeon et al. 2021; Welsh et al. 2021); (ii) an enrichment still dominated by the products of low-energy Population III SNe, but which is transiting toward a C-normal pattern owing to the contribution of subsequent generations of normal (Population II) stars exploding as core-collapse SNe (Salvadori et al. 2015; de Bennassuti et al. 2017; Jeon et al. 2021).

In both cases, the chemical enrichment should be dominated by the chemical products of primordial low-energy SNe, which produce the carbon-over-iron excess (Salvadori et al. 2023). However, CEMP-no relic stars likely form during the first gigayear of cosmic evolution ($z > 6$), while our CEMP-no absorbers are observed at lower redshifts, $z \approx 3$–4, when the universe was >2 Gyr old. What are these CEMP-no absorbers, and how can they preserve the chemical signature of Population III stars?

Two main possibilities exist. The first is that our CEMP-no absorption systems are associated with the diffuse circumgalactic medium of recently born Population III galaxies at $z \approx 3$–4. Still, these objects should be extremely rare. Indeed, direct detection of Population III galaxies is still lacking, and at $z \approx 3$–4 pristine galaxies are expected to be extremely rare (e.g., Pallottini et al. 2014; Jaacks et al. 2019). The second is that our CEMP-no absorption systems are associated with low-mass "sterile" minihalos (Salvadori & Ferrara 2012). Radiative feedback processes can indeed increase the gas temperature of metal-enriched minihalos, which are then too diffuse to form stars but too metal enhanced to be photoevaporated. The chemical signature of the first stellar generations can then be preserved in these gas-rich systems until they evolve in isolation. This physical mechanism, which has been proposed by Salvadori & Ferrara (2012), should be quite common in the early universe and can turn low-mass UFDs at the beginning of their evolution into "failed" UFDs: the gas-rich and high-z dark counterpart of UFDs.

4.2. Comparison with Literature Data

To examine our results in a global context and understand why CEMP-no absorption systems have not been identified yet, we can compare the *total metallicity* of all 37 diffuse absorbers[16] with literature data for LLSs (Fumagalli et al. 2011, 2016; Crighton et al. 2016; Robert et al. 2019). The comparison is shown in Figure 6, where the total metallicity of the absorbers is displayed as a function of redshift (or cosmic time) and our systems are colored to distinguish among [Fe/H] > -2 absorbers, CEMP-no systems, and very metal-poor C-normal absorbers (see caption and Figure 4). Literature data include (i) the four serendipitously discovered LLSs that have $Z < 10^{-3}$ $Z_{\odot}$, covering the same redshift range of our absorbers, $3 < z < 4.5$; and (ii) the sample of LLSs at $0 < z < 4.5$ collected by Fumagalli et al. (2016), for which we report the median metallicity computed by the authors using redshift bins containing at least 25 LLSs.

The right panel of Figure 6 shows the total metallicity distribution function of our absorbers. First, we see that our absorption systems cover a wide metallicity range, 10^{-3} $Z_{\odot} < Z < Z_{\odot}$, and that >90% of our very metal-poor absorbers, [Fe/H] < -2, have a total metallicity $Z < 10^{-2}$ $Z_{\odot}$ (the only exception being one C-normal absorber). This result is a further confirmation that the effect of dust is negligible at [Fe/H] < -2, as suggested by previous works (e.g., Vladilo 1998; Vladilo et al. 2018). Second, we note that the peak of the distribution of our absorption systems, $Z \approx 10^{-2.5}$ $Z_{\odot}$, is in perfect agreement with the average metallicity value of LLSs derived by Fumagalli et al. (2016) in the corresponding redshift bin, $3 < z < 4.5$. Then, we note that among our absorbers there is a lack of extremely metal-poor absorption systems, $Z < 10^{-3}$ $Z_{\odot}$, although our systems cover exactly the same redshift range of the most pristine LLSs. This is certainly due to our initial selection, which was based on the presence of metal absorption lines (see Section 2.1). Finally, we note that CEMP-no absorbers showing the chemical signature of the first stars are *not* the most pristine objects. This result, which is in line with what is found in the stellar halo, is a consequence of the key chemical signature left by primordial low-energy SNe: an excess of C (O, Mg, and Si) over iron. To identify the footprint of primordial low-energy SNe in the gas at high z, we should then look for *the most iron-poor absorbers, which are not the most metal-poor* but rather have 10^{-3} $Z_{\odot} < Z < 10^{-2.3}$ $Z_{\odot}$. Among the 12 absorption systems with available carbon and iron measurements at $Z < 10^{-2.5\pm0.1}$ $Z_{\odot}$, we have that three are CEMP-no, implying that the fraction of CEMP-no systems is $F_{\text{CEMP-no}}(Z < 10^{-2.5}$ $Z_{\odot}) \geqslant 25\%$. We note that this is just an indicative fraction since we have not determined the completeness of our selection of absorption systems based on the automatic detection of Mg II absorption doublets.

Ultimately, we suggest that metal-poor LLSs are the most promising candidates as CEMP-no absorption systems. Indeed, on the one hand, DLAs are likely too dense to stop forming stars and thus are naturally dominated by the chemical products of normal Population II stars. On the other hand, the most pristine LLSs are too metal-poor to be enriched by the chemical products of primordial low-energy SNe.

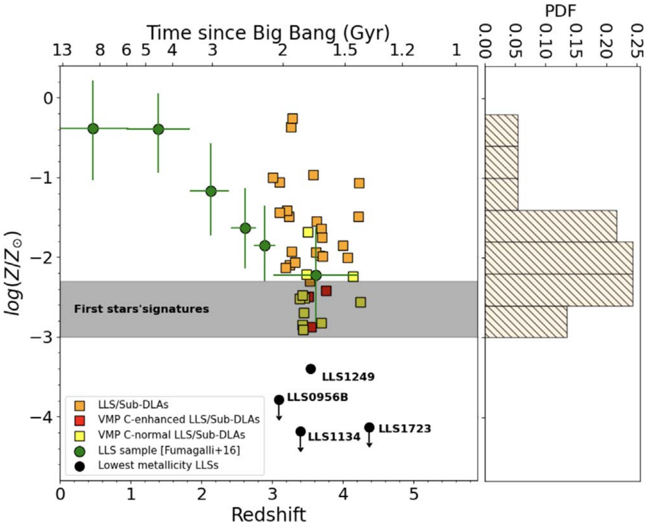

Figure 6. Summary of the metallicity distribution of LLSs (green and black circles) in the literature. Upper limits from Fumagalli et al. (2011) for two apparently metal-free LLSs, LLS0958B65 and LLS113465, and from Robert et al. (2019), LLS172366, are shown with black arrows. The lowest metallicity measurement for an LLS from Crighton et al. (2016), LLS124967, is shown in black. The green circles and error bars represent the LLS sample of Fumagalli et al. (2016). Red and yellow squares are C-enhanced and C-normal very metal-poor absorbers, respectively. Orange squares are iron-rich absorbers. The shaded red region shows the metallicity range, according to our results, for gas enriched by first stars. On the right we show the metallicity posterior distribution function of all our absorbers.

5. Conclusions

In this paper, we have studied the chemical abundances of 37 optically thick Lyα absorbers (LLSs and sub-DLAs) at $z \sim 3$–4.5 identified in the spectra of the XQ-100 quasar legacy survey (López et al. 2016). Column densities of the absorption features have been derived through fitting with Voigt profiles, and ionization corrections have been applied in order to derive the chemical abundances. The main results of our study can be summarized as follows:

1. The MDF of our absorption systems covers a broad range in iron abundance and is bimodal: it has a broad peak at [Fe/H] ~ -0.8 and a more pronounced one at [Fe/H] ~ -2.
2. The low-Fe tail of the MDF of our absorption systems almost overlaps with the stellar MDF observed in UFDs.
3. Among the 30 analyzed absorbers with available iron measurements, we identified 14 very metal-poor systems, [Fe/H] < -2, three of which are carbon-enhanced, [C/Fe] $> +0.7$ (J0835+0650 at $z = 3.51256$, J1111−0804 at $z = 3.75837$, and J1658−0739 at $z = 3.54604$).
4. The chemical abundance ratios (C, O, Mg, and Si over Fe) measured in very metal-poor absorbers are in good agreement with those of very metal-poor stars in the Galactic halo and dwarf galaxies.
5. Conversely, at [Fe/H] > -2, the absorbers' abundance ratios exhibit a larger scatter than present-day stars, suggesting that dust contribution is no longer negligible at these [Fe/H] values.

---

[16] Note that the number of absorption systems with iron measurements is smaller (30) than those with metallicity measurements.

6. The three C-enhanced very metal-poor absorbers also show an overabundance of Mg and Si, which are produced by first stars exploding as low-energy SNe and not by AGB stars. These overabundances are also observed in CEMP-no stars.
7. All C-enhanced very metal-poor absorption systems have $A(\mathrm{C}) < 7.4$, i.e., they reside in the so-called low carbon band, as is observed for CEMP-no stars.
8. Conversely, all C-enhanced systems at $[\mathrm{Fe/H}] > -2$ dwell in the high carbon band, $A(\mathrm{C}) > 7.4$, consistent with CEMP-*s* stars.
9. CEMP-no absorbers are the most iron-poor among our diffuse systems, but they are not the most metal-poor ones.
10. Among the 12 absorption systems with available C and Fe measurements at $Z < 10^{-2.5\pm0.1}\,Z_{\odot}$, we have that three are CEMP-no, implying that $F_{\text{CEMP-no}}(Z < 10^{-2.5}\,Z_{\odot}) \geqslant 25\%$.

Ultimately, our CEMP-no absorption systems seem to be the gaseous high-redshift analogs of locally observed CEMP-no stars, which have been more likely imprinted by primordial low-energy SNe. Our new discovery of CEMP-no absorbers suggests that optically thick, relatively diffuse absorption systems are the best environments to identify the missing chemical signature of the first stellar generations in the gaseous component. These absorbers are likely too diffuse to be star-forming, a key requirement to prevent further chemical pollution and thus to preserve the first-star signature. Theoretical investigations and further observational studies are required to fully understand their nature.

In the very near future, extremely large samples of high-redshift quasars will be available from several surveys (DESI, Abareshi et al. 2022; WEAVE-QSO, Pieri et al. 2016; 4-MOST, de Jong et al. 2019). They will allow us to select more of these CEMP-no absorbers to statistically characterize their properties and number density. A significant step forward in the analysis of these systems will be represented by ANDES, the high-resolution ($R \sim 100{,}000$) spectrograph for the Extremely Large Telescope (ELT), foreseen for the beginning of the 2030s (Marconi et al. 2022). The ANDES spectral coverage extending to the NIR and the collecting power of ELT will allow us to carry out detailed studies of these systems resolving the metal absorptions and determining significant constraints on key elements like Zn.

In the end, our work, which fully complements stellar archeology, represents a fresh start for the searches of first-star pollution in high-z environments that can provide unique insight on both the early phases of reionization and the physical processes shaping the evolution of the first galaxies (Salvadori & Ferrara 2012; Pallottini et al. 2014).

This project has received funding from the European Research Council (ERC) under the European Union's Horizon 2020 research and innovation program (grant agreement No. 804240; PI S. Salvadori). A.S. acknowledges support from ED127 and DIM-ACAV+; S.S. and V.D. from the PRIN-MIUR17, the quest for the first stars, prot. no. 2017T4ARJ5; M.F. from the ERC Starting Grant FEEDGALAXIES H2020/757535; G.B. was supported by the National Science Foundation through grant AST-1751404; and S.L. was funded by FONDECYT grant No. 1231187. The authors are grateful to Stefano Cristiani, Paolo Molaro, Asa Skuladottir, Monique Spite, Irene Vanni, Susanna D. Vergani, and Louise Welsh for insightful discussions and critical reading of the first draft of the manuscript. We thank the referee, Timothy Beers, for an enthusiastic report.

Appendix
Supplemental Material

In this Appendix we show the results of the Voigt profile fitting of two very metal-poor absorption systems (Figure 7). We also show a portion of the Voigt fit parameters table for guidance (Table 6). The complete figure set and the entire table are available online as supplemental material.

J0211+1107 z3.50250

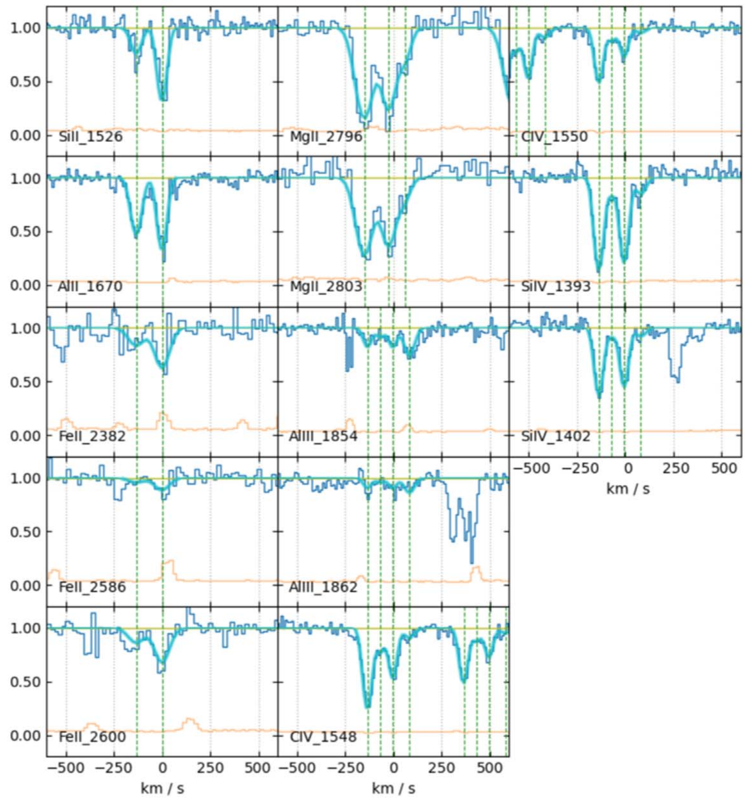

J0247-0556 z4.13952

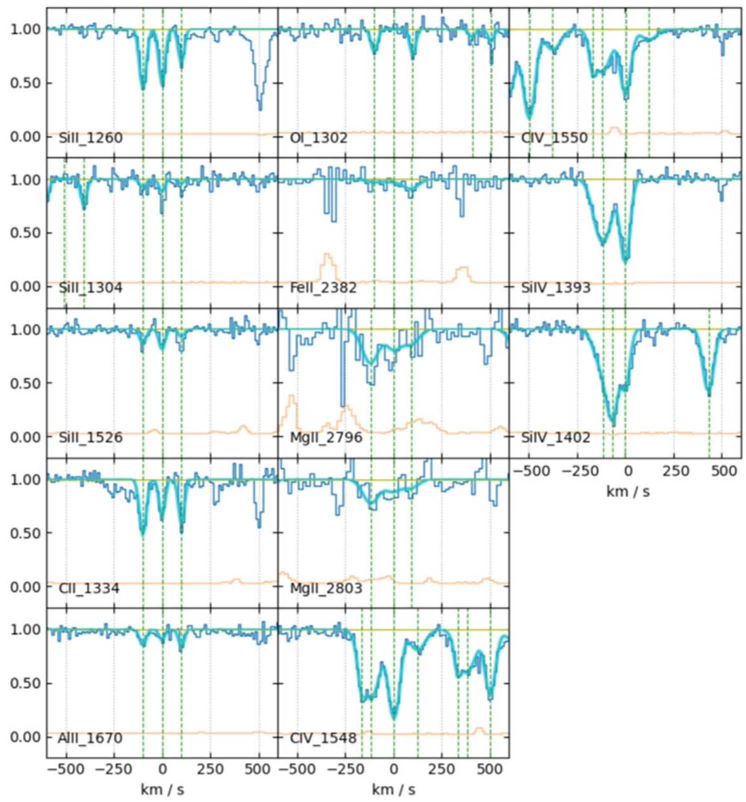

Figure 7. Voigt fit profile of J0211+1107 at $z = 3.50250$ and J0247−0556 at $z = 4.13952$. Data are in blue, the fit is in cyan, the error spectrum is in orange, the continuum level is in yellow, and the vertical green dashed lines indicate the center of the components.

(The complete figure set (7 images) is available.)

Table 6
Voigt Fit Parameters

System	Transition	Redshift	$\log N$	$\Delta \log N$	b	Δb
J0211+1107 z3.50250						
	MgII-2796.MgII-2803	3.5014070	13.719	0.046	37.773	1.987
	AlII-1670	3.5016674	12.825	0.025	37.773	1.987
	SiII-1526	3.5016674	13.548	0.090	37.773	1.987
	FeII-2344.FeII-2382.FeII-2586.FeII-2600	3.5016674	12.992	0.078	37.773	1.987
	SiIV-1393.SiIV-1402	3.5016728	13.759	0.018	28.752	0.983
	CIV-1548.CIV-1550	3.5016728	14.021	0.017	28.752	0.983
	AlIII-1854.AlIII-1862	3.5016728	12.623	0.066	28.752	0.983
	SiIV-1393.SiIV-1402	3.5035909	13.661	0.020	29.551	1.503
	CIV-1548.CIV-1550	3.5035909	13.682	0.026	29.551	1.503
	AlIII-1854.AlIII-1862	3.5035909	12.641	0.071	29.551	1.503
	CIV-1548.CIV-1550	3.5026589	13.216	0.082	23.373	7.591
	SiIV-1393.SiIV-1402	3.5026589	12.647	0.129	23.373	7.591
	AlIII-1854.AlIII-1862	3.5026589	12.221	0.141	23.373	7.591
	MgII-2796.MgII-2803	3.5033051	13.671	0.061	28.884	1.607
	AlII-1670	3.5036733	12.922	0.028	28.884	1.607
	SiII-1526	3.5036733	13.952	0.038	28.884	1.607
	FeII-2344.FeII-2382.FeII-2586.FeII-2600	3.5036733	13.397	0.047	28.884	1.607
	MgII-2796.MgII-2803	3.5045587	12.976	0.166	9.951	4.374
	SiIV-1393.SiIV-1402	3.5049457	12.718	0.097	30.884	5.803
	CIV-1548.CIV-1550	3.5049457	12.857	0.131	30.884	5.803
	AlIII-1854.AlIII-1862	3.5049457	12.838	0.067	30.884	5.803
J0247−0556 z4.13952						
	CIV-1548.CIV-1550	4.1355034	13.644	0.167	6.000	2.703
	CIV-1548.CIV-1550	4.1363172	14.153	0.019	54.048	3.693
	SiIV-1393.SiIV-1402	4.1363915	13.685	0.022	54.048	3.693
	SiII-1260.SiII-1304.SiII-1526	4.1366451	13.058	0.043	12.487	1.721
	CII-1334	4.1366451	13.938	0.050	12.487	1.721
	OI-1302	4.1366451	13.819	0.082	12.487	1.721
	AlII-1670	4.1366451	11.953	0.090	12.487	1.721
	FeII-2382	4.1366451	12.170	0.150	12.487	1.721
	MgII-2796.MgII-2803	4.1363254	12.937	0.179	12.487	1.721
	SiII-1260.SiII-1304.SiII-1526	4.1383433	13.243	0.091	7.412	0.601
	CII-1334	4.1383433	13.720	0.087	7.412	0.601
	AlII-1670	4.1383433	11.749	0.160	7.412	0.601
	MgII-2796.MgII-2803	4.1383433	12.985	0.179	7.412	0.601
	FeII-2382	4.1383433	12.326	0.150	7.412	0.601
	OI-1302	4.1383433	11.819	0.082	7.412	0.601
	SiIV-1393.SiIV-1402	4.1383660	13.687	0.027	23.871	2.021
	CIV-1548.CIV-1550	4.1384004	14.182	0.014	23.871	2.021
	MgII-2796.MgII-2803	4.1399028	12.634	0.136	10.000	0.000
	FeII-2382	4.1399028	12.741	0.192	10.000	0.000
	SiII-1260.SiII-1304.SiII-1526	4.1400627	12.750	0.091	7.000	0.000
	CII-1334	4.1400627	13.879	0.132	7.000	0.000
	OI-1302	4.1400627	13.908	0.150	7.000	0.000
	AlII-1670	4.1400627	11.974	0.150	7.000	0.000
	CIV-1548.CIV-1550	4.1404764	13.444	0.047	43.605	8.025

(This table is available in its entirety in machine-readable form.)

ORCID iDs

Andrea Saccardi https://orcid.org/0000-0002-6950-4587
Stefania Salvadori https://orcid.org/0000-0001-7298-2478
Valentina D'Odorico https://orcid.org/0000-0003-3693-3091
Guido Cupani https://orcid.org/0000-0002-6830-9093
Michele Fumagalli https://orcid.org/0000-0001-6676-3842
Trystyn A. M. Berg https://orcid.org/0000-0002-2606-5078
George D. Becker https://orcid.org/0000-0003-2344-263X
Sara Ellison https://orcid.org/0000-0002-1768-1899
Sebastian Lopez https://orcid.org/0000-0003-0389-0902

References

Abareshi, B., Aguilar, J., Ahlen, S., et al. 2022, AJ, 164, 207
Abate, C., Pols, O. R., Izzard, R. G., & Karakas, A. I. 2015, A&A, 581, A22
Aguado, D., Molaro, P., Caffau, E., et al. 2022, A&A, 668, A86
Aguado, D. S., Caffau, E., Molaro, P., et al. 2023, A&A, 669, L4
Aguado, D. S., González Hernández, J. I., Allende Prieto, C., & Rebolo, R. 2019, ApJL, 874, L21
Amarsi, A. M., Nissen, P. E., & Skúladóttir, Á. 2019, A&A, 630, A104
Andrievsky, S. M., Spite, M., Korotin, S. A., et al. 2010, A&A, 509, A88
Arentsen, A., Starkenburg, E., Shetrone, M. D., et al. 2019, A&A, 621, A108
Asplund, M., Grevesse, N., Sauval, A. J., & Scott, P. 2009, ARA&A, 47, 481
Beers, T. C., & Christlieb, N. 2005, ARA&A, 43, 531
Beers, T. C., Preston, G. W., & Shectman, S. A. 1992, AJ, 103, 1987

Berg, T. A. M., Ellison, S. L., Prochaska, J. X., et al. 2017, MNRAS, 464, L56
Berg, T. A. M., Ellison, S. L., Sánchez-Ramírez, R., et al. 2016, MNRAS, 463, 3021
Berg, T. A. M., Ellison, S. L., Sánchez-Ramírez, R., et al. 2019, MNRAS, 488, 4356
Berg, T. A. M., Fumagalli, M., D'Odorico, V., et al. 2021, MNRAS, 502, 4009
Bonifacio, P., Caffau, E., Spite, M., et al. 2015, A&A, 579, A28
Bonifacio, P., Caffau, E., Spite, M., et al. 2018, A&A, 612, A65
Bonifacio, P., Molaro, P., Beers, T. C., & Vladilo, G. 1998, A&A, 332, 672
Bonifacio, P., Monaco, L., Salvadori, S., et al. 2021, A&A, 651, A79
Bonifacio, P., Spite, M., Cayrel, R., et al. 2009, A&A, 501, 519
Bromm, V., & Loeb, A. 2003, Natur, 425, 812
Carswell, R. F., Becker, G. D., Jorgenson, R. A., Murphy, M. T., & Wolfe, A. M. 2012, MNRAS, 422, 1700
Cayrel, R., Depagne, E., Spite, M., et al. 2004, A&A, 416, 1117
Chiaki, G., Tominaga, N., & Nozawa, T. 2017, MNRAS, 472, L115
Christensen, L., Vergani, S. D., Schulze, S., et al. 2017, A&A, 608, A84
Christlieb, N., Bessell, M. S., Beers, T. C., et al. 2002, Natur, 419, 904
Cooke, R., Pettini, M., & Murphy, M. T. 2012, MNRAS, 425, 347
Cooke, R., Pettini, M., Steidel, C. C., Rudie, G. C., & Jorgenson, R. A. 2011a, MNRAS, 412, 1047
Cooke, R., Pettini, M., Steidel, C. C., Rudie, G. C., & Nissen, P. E. 2011b, MNRAS, 417, 1534
Crighton, N. H. M., O'Meara, J. M., & Murphy, M. T. 2016, MNRAS, 457, L44
Cupani, G., D'Odorico, V., Cristiani, S., et al. 2020, Proc. SPIE, 11452, 372
de Bennassuti, M., Salvadori, S., Schneider, R., Valiante, R., & Omukai, K. 2017, MNRAS, 465, 926
De Cia, A., Ledoux, C., Petitjean, P., & Savaglio, S. 2018, A&A, 611, A76
de Jong, R. S., Agertz, O., Berbel, A. A., et al. 2019, Msngr, 175, 3
D'Odorico, V., Cristiani, S., Pomante, E., et al. 2016, MNRAS, 463, 2690
D'Odorico, V., Finlator, K., Cristiani, S., et al. 2022, MNRAS, 512, 2389
Dutta, R., Srianand, R., Rahmani, H., et al. 2014, MNRAS, 440, 307
Ferland, G. J., Chatzikos, M., Guzmán, F., et al. 2017, RMxAA, 53, 385
François, P., Caffau, E., Wanajo, S., et al. 2018, A&A, 619, A10
Frebel, A., Aoki, W., Christlieb, N., et al. 2005, Natur, 434, 871
Frebel, A., & Norris, J. E. 2015, ARA&A, 53, 631
Fumagalli, M., O'Meara, J. M., & Prochaska, J. X. 2011, Sci, 334, 1245
Fumagalli, M., O'Meara, J. M., & Prochaska, J. X. 2016, MNRAS, 455, 4100
González Hernández, J. I., Aguado, D. S., Allende Prieto, C., Burgasser, A. J., & Rebolo, R. 2020, ApJL, 889, L13
Haardt, F., & Madau, P. 2012, ApJ, 746, 125
Hansen, T. T., Andersen, J., Nordström, B., et al. 2016a, A&A, 586, A160
Hansen, T. T., Andersen, J., Nordström, B., et al. 2016b, A&A, 588, A3
Hartwig, T., Yoshida, N., Magg, M., et al. 2018, MNRAS, 478, 1795
Heger, A., & Woosley, S. E. 2002, ApJ, 567, 532
Heger, A., & Woosley, S. E. 2010, ApJ, 724, 341
Hirano, S., Hosokawa, T., Yoshida, N., et al. 2014, ApJ, 781, 60
Hosokawa, T., Omukai, K., Yoshida, N., & Yorke, H. W. 2011, Sci, 334, 1250
Iršič, V., Viel, M., Berg, T. A. M., et al. 2017a, MNRAS, 466, 4332
Iršič, V., Viel, M., Haehnelt, M. G., et al. 2017b, PhRvD, 96, 023522
Iwamoto, N., Umeda, H., Tominaga, N., Nomoto, K., & Maeda, K. 2005, Sci, 309, 451
Jaacks, J., Finkelstein, S. L., & Bromm, V. 2019, mnras, 488, 2202
Jeon, M., Bromm, V., Besla, G., Yoon, J., & Choi, Y. 2021, mnras, 502, 1
Ji, A. P., Frebel, A., Ezzeddine, R., & Casey, A. R. 2016, ApJL, 832, L3
Karakas, A. I., & Lattanzio, J. C. 2014, PASA, 31, e030
Keller, S. C., Bessell, M. S., Frebel, A., et al. 2014, Natur, 506, 463
Lee, Y. S., Beers, T. C., Masseron, T., et al. 2013, AJ, 146, 132
Limongi, M., & Chieffi, A. 2018, ApJS, 237, 13
Liu, B., Sibony, Y., Meynet, G., & Bromm, V. 2021, MNRAS, 506, 5247
Lofthouse, E. K., Fumagalli, M., Fossati, M., et al. 2023, MNRAS, 518, 305
López, S., D'Odorico, V., Ellison, S. L., et al. 2016, A&A, 594, A91
Lucatello, S., Beers, T. C., Christlieb, N., et al. 2006, ApJL, 652, L37
Lucatello, S., Tsangarides, S., Beers, T. C., et al. 2005, ApJ, 625, 825
Marassi, S., Chiaki, G., Schneider, R., et al. 2014, ApJ, 794, 100
Marconi, A., Abreu, M., Adibekyan, V., et al. 2022, Proc. SPIE, 12184, 1218424
Marsteller, B., Beers, T. C., Rossi, S., et al. 2005, NuPhA, 758, 312
Murphy, M. T., Kacprzak, G. G., Savorgnan, G. A. D., & Carswell, R. F. 2019, MNRAS, 482, 3458
Norris, J. E., Ryan, S. G., & Beers, T. C. 1997, ApJL, 489, L169
Norris, J. E., Yong, D., Bessell, M. S., et al. 2013, ApJ, 762, 28
Pallottini, A., Ferrara, A., Gallerani, S., Salvadori, S., & D'Odorico, V. 2014, MNRAS, 440, 2498
Perrotta, S., D'Odorico, V., Hamann, F., et al. 2018, MNRAS, 481, 105
Perrotta, S., D'Odorico, V., Prochaska, J. X., et al. 2016, MNRAS, 462, 3285
Pieri, M. M., Bonoli, S., Chaves-Montero, J., et al. 2016, in SF2A-2016: Proc. Annual Meeting of the French Society of Astronomy and Astrophysics, ed. C. Reylé et al., 259
Placco, V. M., Frebel, A., Beers, T. C., & Stancliffe, R. J. 2014, ApJ, 797, 21
Placco, V. M., Roederer, I. U., Lee, Y. S., et al. 2021, ApJL, 912, L32
Placco, V. M., Santucci, R. M., Beers, T. C., et al. 2019, ApJ, 870, 122
Quiret, S., Péroux, C., Zafar, T., et al. 2016, MNRAS, 458, 4074
Robert, P. F., Murphy, M. T., O'Meara, J. M., Crighton, N. H. M., & Fumagalli, M. 2019, MNRAS, 483, 2736
Rossi, S., Beers, T. C., Sneden, C., et al. 2005, AJ, 130, 2804
Salvadori, S., Bonifacio, P., Caffau, E., et al. 2019, MNRAS, 487, 4261
Salvadori, S., & Ferrara, A. 2012, MNRAS, 421, L29
Salvadori, S., Skúladóttir, Á., & Tolstoy, E. 2015, MNRAS, 454, 1320
Salvadori, S., D'Odorico, V., Saccardi, A., Skúladóttir, Á., & Vanni, I. 2023, MemSAIt, in press
Sánchez-Ramírez, R., Ellison, S. L., Prochaska, J. X., et al. 2016, MNRAS, 456, 4488
Schneider, R., Ferrara, A., Salvaterra, R., Omukai, K., & Bromm, V. 2003, Natur, 422, 869
Simon, J. D. 2019, ARA&A, 57, 375
Skúladóttir, Á., Salvadori, S., Amarsi, A. M., et al. 2021, ApJL, 915, L30
Skúladóttir, Á., Salvadori, S., Pettini, M., Tolstoy, E., & Hill, V. 2018, A&A, 615, A137
Spite, M., Caffau, E., Bonifacio, P., et al. 2013, A&A, 552, A107
Spite, M., Spite, F., François, P., et al. 2018, A&A, 617, A56
Starkenburg, E., Aguado, D. S., Bonifacio, P., et al. 2018, MNRAS, 481, 3838
Starkenburg, E., Shetrone, M. D., McConnachie, A. W., & Venn, K. A. 2014, MNRAS, 441, 1217
Suda, T., Katsuta, Y., Yamada, S., et al. 2008, PASJ, 60, 1159
Takahashi, K., Yoshida, T., & Umeda, H. 2018, ApJ, 857, 111
Vernet, J., Dekker, H., D'Odorico, S., et al. 2011, A&A, 536, A105
Vladilo, G. 1998, ApJ, 493, 583
Vladilo, G., Gioannini, L., Matteucci, F., & Palla, M. 2018, ApJ, 868, 127
Welsh, L., Cooke, R., & Fumagalli, M. 2019, MNRAS, 487, 3363
Welsh, L., Cooke, R., & Fumagalli, M. 2021, MNRAS, 500, 5214
Welsh, L., Cooke, R., Fumagalli, M., & Pettini, M. 2022, ApJ, 929, 158
Yong, D., Norris, J. E., Bessell, M. S., et al. 2013, ApJ, 762, 27
Yoon, J., Beers, T. C., Dietz, S., et al. 2018, ApJ, 861, 146
Yoon, J., Beers, T. C., Placco, V. M., et al. 2016, ApJ, 833, 20
Yoon, J., Beers, T. C., Tian, D., & Whitten, D. D. 2019, ApJ, 878, 97
Zepeda, J., Beers, T. C., Placco, V. M., et al. 2022, arXiv:2209.12224
Zou, S., Petitjean, P., Noterdaeme, P., et al. 2020, ApJ, 901, 105